Sustainable thick nanodiamond composite coatings on hard metal: effects of varied discharge energies on tribological performance and corrosion resistance.

MOHAMED, A., FARGHALI, A. A., KHALIL, A. M., ABDEL-WAHAB, M. S., TAWFIK, W. Z., SAEED, A. A., DIAB, M. R., MURASAWA, K., NARAGINO, H., YOSHITAKE, T., and EGIZA, M.

2025

Surface & Coatings Technology 498 (2025) 131844

Contents lists available at ScienceDirect

Surface & Coatings Technology

journal homepage: www.elsevier.com/locate/surfcoat

Sustainable thick nanodiamond composite coatings on hard metal: Effects of varied discharge energies on tribological performance and corrosion resistance

Alaaeldin Mohamed [a], Ahmed A. Farghali [a], Ahmed M.E. Khalil [b,c], Mohamed Sh. Abdel-Wahab [a], Wael Z. Tawfik [d], Ayman Ali Saeed [e], Mohamed Ragab Diab [f,g], Koki Murasawa [g], Hiroshi Naragino [g], Tsuyoshi Yoshitake [g,*], Mohamed Egiza [f,h,**]

[a] Materials Science and Nanotechnology Department, Faculty of Postgraduate Studies for Advanced Sciences, Beni–Suef University, Beni–Suef 62511, Egypt
[b] Faculty of Environment, Science and Economy, University of Exeter, Exeter EX4 4QF, UK
[c] Department of Chemical Engineering, Faculty of Engineering, Cairo University, Giza 12613, Egypt
[d] Department of Physics, Faculty of Science, Beni-Suef University, Beni-Suef 62511, Egypt
[e] Applied Organic Chemistry Department, Chemical Industries Research Institute, National Research Centre (NRC), Dokki, Giza 12622, Egypt
[f] Department of Mechanical Engineering, Kafrelsheikh University, Kafrelsheikh 33516, Egypt
[g] Department of Advanced Energy Science and Engineering, Faculty of Engineering Sciences, Kyushu University, Kasuga, Fukuoka 816-8580, Japan
[h] School of Computing, Engineering and Technology, Robert Gordon University, Garthdee Road, Aberdeen AB10 7GJ, UK

ARTICLE INFO

Keywords:
Wear resistance
Low friction
Corrosion resistance
Sustainable coatings
Arc plasma
Hardness

ABSTRACT

Sustainable nanodiamond composite (NDC) coatings were deposited on WC – 6%Co substrates using eco-friendly Coaxial Arc Plasma Deposition method at discharge energies of 3.6–9.0 J/pulse. This study optimized discharge energy to enhance adhesion strength, wear resistance, and corrosion resistance, promoting sustainability in preparation and operation of coated cutting tools. NDC coatings, produced without external heating, chemical gases, or cobalt chemical etching, achieved 16 μm thickness with deposition rates ranging from 3.2 to 5.7 μm/h, exhibiting dense and pore-free structures. Hardness peaked at 72.5 GPa at 7.0 J/pulse, slightly decreasing to 65 GPa at 9.0 J/pulse, with Young's modulus showing similar trends. Maximum adhesion strength was 42.5 N achieved at 9.0 J/pulse, attributed to suppressed internal stress at the interface. Wear resistance improved significantly, with wear rates peaking at 1.88E-7 mm^3/N·m at 7.0 J/pulse, aligning with hardness and C sp^3 content from Raman analysis. The coatings exhibited a low coefficient of friction (0.09), representing a sevenfold reduction compared to uncoated substrates, due to an sp^2-rich transfer layer enabling enhanced sliding properties. Corrosion resistance improved in 3.5 wt% NaCl solution, achieving 0.5136 mil/year at 7.0 J/pulse, a 60.4 % improvement, though reduced at 9.0 J/pulse due to presence of larger cauliflower-like particles allowing solution penetration. These results highlight NDC coatings as a sustainable and high-performance alternative coating for WC−6%Co cutting tools.

1. Introduction

Cemented carbide (WC−Co) composites have become essential materials in various industries due to their outstanding toughness, and tribological properties [1,2]. These composites play a vital role in the oil and gas drilling process and manufacturing sector, especially in cutting tools used to machine challenging materials like Al—Si alloys, SiC, and carbon fibre-reinforced polymers [3]. Despite their widespread use and benefits, WC−Co composites face significant limitations regarding wear and corrosion resistance, particularly under harsh operating conditions [4].

Localized temperature increases during cutting or drilling can lead to oxidation and subsequent material degradation, especially of the Co binder phase [5]. Furthermore, exposure to corrosive environments, such as coolants or seawater, exacerbates these challenges [6]. The heterogeneous composition of WC−6%Co composites, consisting of

* Corresponding author.
** Correspondence to: M. Egiza, Department of Mechanical Engineering, Kafrelsheikh University, Kafrelsheikh 33516, Egypt.
E-mail addresses: Tsuyoshi_yoshitake@kyudai.jp (T. Yoshitake), Mohamed_Egiza@eng.kfs.edu.eg (M. Egiza).

https://doi.org/10.1016/j.surfcoat.2025.131844
Received 1 November 2024; Received in revised form 19 January 2025; Accepted 22 January 2025
Available online 23 January 2025

multiple carbide phases and a metallic binder, renders them exposed to galvanic corrosion, wherein the Co binder preferentially dissolves, compromising the integrity of the composite [7]. This tendency to corrosion significantly weakens mechanical properties, raising concerns about operational efficiency and increasing maintenance costs [8].

The presence of cobalt in WC−Co composites raises concerns regarding its tendency to galvanic corrosion, especially in aggressive environments such as seawater or mining operations [1]. For instance, in WC−Co composites, cobalt functions as a binder but preferentially corrodes (oxidises) as an anode in aggressive environments (when in contact with more noble metal or mineral as a cathode), resulting in galvanic corrosion that compromises the composite by leaving WC particles unsupported. The pH of the electrolyte significantly influences the corrosion behaviour of WC−Co cemented carbides. Active dissolution of the cobalt binder occurs in acidic and neutral electrolytes, while dissolution of WC occurs in alkaline electrolytes. This creates the potential for galvanic corrosion between these phases, wherein the interaction of two materials with differing corrosion potentials in a solution leads to galvanic coupling and the dissolution of the less noble material [9,10]. Additionally, addressing cobalt toxicity is vital, necessitating the development of alternative binders or the application of surface coatings that enhance corrosion resistance without compromising mechanical integrity [8,11].

To address these challenges, coatings with specific attributes are essential for prolonging the lifespan and enhancing the performance of cutting tools [12]. These attributes include high hardness, low friction coefficients, and excellent corrosion resistance. The machining environment presents significant requirements, as cutting tools are subjected to extreme temperatures up to 1000 °C, considerable wear and friction, and exposure to corrosive and oxidative conditions [13]. Consequently, wear-resistant hard coatings are commonly applied to ensure tool durability. The industry's ongoing push for greater cost-efficiency and productivity necessitates higher cutting speeds and feed rates, which further requires coatings that contribute to longer tool lifespans [14].

These considerations highlight the urgent need for advanced protective coatings specifically designed to withstand demanding working conditions. Surface hard coatings, including TiN, TiCN, TiAlN, TiN/TiCN/TiC/TiN, TiN/TiCN/TiC/Al_2O_3 [1,15], diamond-like carbon (DLC) [16], and diamond coatings [17], have demonstrated promise in improving corrosion resistance and extending the lifespan of WC − 6% Co components. However, the widespread application of diamond and related carbon coatings, such as DLC, is limited due to factors such as restricted adhesion and film thickness [18]. Additional barriers include high costs, slow deposition rates, potential chemical hazards during deposition, the requirement for chemical etching of Co during substrate surface pretreatment, and the necessity for high deposition temperatures in diamond coatings [19].

The catalytic formation of graphite presents a significant challenge during the chemical vapor deposition (CVD) of diamond films on substrates containing iron, cobalt, and nickel, particularly due to the high deposition temperatures (≥800 °C) [20]. Cobalt, as a transition metal, is known for its catalytic effects, which can lead to diamond graphitization [21,22] and deterioration of film adhesion [23,24]. Therefore, suppressing the catalytic effects of Co at the interface and enabling low-temperature deposition of cost-effective diamond and related alternative hard-carbon coatings are crucial for producing WC−6%Co cutting tools that exhibit high coatings' hardness, good adhesion, and low coefficients of friction (COF), suitable for machining difficult-to-cut materials.

Research efforts increasingly emphasize sustainable development and environmentally conscious practices within the manufacturing sector [25]. Consequently, there is a growing focus on minimizing energy consumption, reducing fabrication costs, and eliminating the use of hazardous chemicals during coating synthesis [26,27]. In this context, nanodiamond composite (NDC) films have emerged as a promising solution [28]. These films comprise two carbon phases: nanodiamond crystals and an amorphous carbon (a-C) matrix [29,30]. NDC films combine the advantageous properties of diamond and DLC coatings while overcoming their limitations and avoiding the adverse environmental impacts associated with conventional CVD methods.

Coaxial Arc Plasma Deposition (CAPD), an environmentally friendly physical vapor deposition (PVD) technique, offers significant advantages over conventional methods. Compared to CVD, CAPD operates at lower deposition temperatures, achieves faster growth rates, and lower costs [31]. Additionally, it enables the creation of sharper cutting edges and provides precise control over film thickness. CAPD technique can deposit NDC films on WC − 6%Co substrates at room substrate-temperature, thereby minimizing Co diffusion, a common concern in CVD techniques [32]. Furthermore, NDC coatings deposited via CAPD tend to exhibit a dense structure characterized by a high content of sp^3-bonded carbon, making them comparable to amorphous diamond [28,33].

The dense structure of NDC films serves as a barrier to inhibit Co diffusion, consisting of a high proportion of sp^3 bonds from the diamond nanocrystals and the a-C matrix [34]. NDC films deposited through CAPD present distinct advantages over traditional methods, as they can adhere directly to WC − 6%Co substrates without requiring chemical etching of Co or external heating, all within a clean vacuum environment devoid of chemical reactions [35]. This approach eliminates environmental, and safety concerns associated with chemical etching, as well as energy consumption related to external heating. Furthermore, NDC coatings demonstrate exceptional mechanical characteristics, such as high hardness, smooth surface, and outstanding wear resistance, making them suitable for diverse tribological applications [36,37].

Previous studies have established a positive correlation between discharge power (ranging from 1.8 J/pulse to 144.0 J/pulse) and enhanced plasma saturation, accompanied by an increase in nanodiamond crystal size from 2.4 nm to 15.0 nm [38]. Recent investigations into the effects of discharge energy on film hardness revealed that 7 J/pulse is the optimal energy for enhancing NDC film hardness [39]. However, the tribological properties, corrosion resistance, and potential for thicker films for enhanced durability remain unexplored.

In this study, NDC coatings were deposited on WC − 6%Co substrates using CAPD from a pure solid-graphite target at discharge energies ranging from 3.6 to 9.0 J/pulse. The deposition process was carried out in a vacuum atmosphere, eliminating the need for external substrate heating or cobalt etching from the substrate surface. The tribological properties and corrosion resistance of both NDC-coated and uncoated WC − 6%Co substrates were systematically evaluated, with results correlated to their mechanical and structural characteristics.

2. Experimental methods

2.1. Films preparation

Prior to deposition, WC − 6 % Co substrates; flat (10 mm diameter, 5.5 mm thick) and pin (ϕ 6 mm diameter, 20 mm length) with spherical end were roughened (Ra: 0.25–0.3 μm) to promote adhesion between the film and substrate. Subsequently, the substrates underwent a thorough cleaning process involving a three-step ultrasonic treatment with acetone, methanol, and pure water for 7 min each to remove any surface contaminants.

A thick single-layer NDC film was subsequently deposited onto the prepared substrates using CAPD as shown in Fig. 1. The CAPD system utilized a high-purity (99.99 %) graphite rod (φ10 × 30 mm) as the cathode within an ULVAC coaxial arc plasma gun (APG-1000, Japan). The end of anodic cylinder to substrate-holder was fixed at 20 mm. To maintain a clean and controlled deposition environment, the CAPD chamber was evacuated to a pressure below 10^{-4} Pa before the process commenced. During deposition, the arc plasma gun operated at discharge energies of 3.6, 5.2, 7.0, and 9.0 J/pulse, utilizing a 720 μF capacitor and a frequency of 1 Hz in a vacuum atmosphere, without

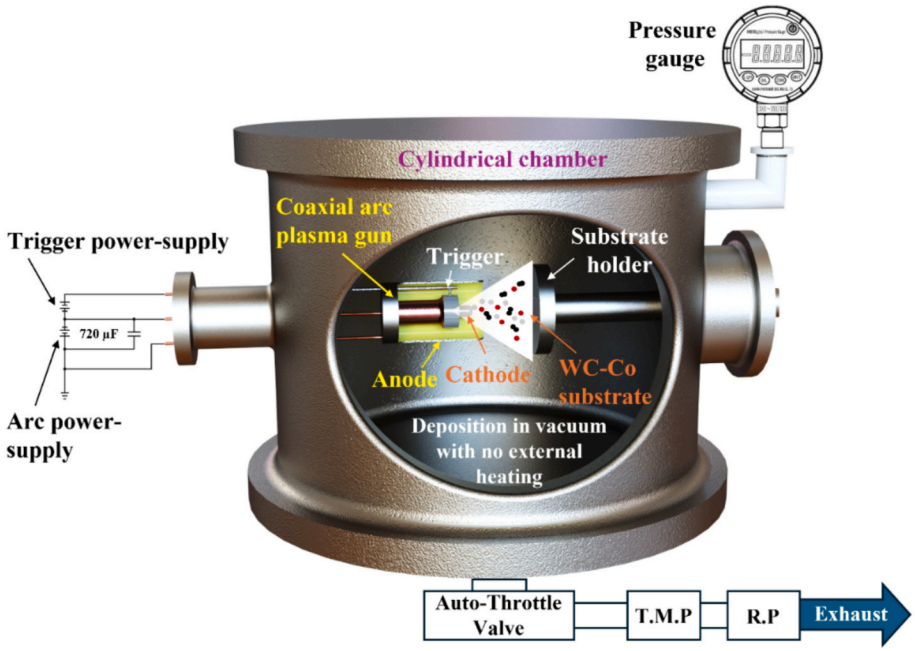

Fig. 1. Schematic diagram of Coaxial Arc Plasma Deposition (CAPD) technique.

external substrate heating. The substrate temperature increased to a maximum of approximately 100 °C due to energy transfer from the plasma, particularly at higher discharge energies, where the plasma plume approached the substrate surface.

2.2. Films characterization

Various techniques were employed to characterize the deposited NDC films. Energy-dispersive X-ray spectroscopy (EDX) in conjunction with field emission scanning electron microscopy (FE-SEM, JEOL, JSM-IT700HR) was used to determine the film thickness and analyse its elemental composition. This analysis was conducted on both the top surface and cross-sections of the film using a depth profiling technique to achieve a comprehensive compositional profile. Additionally, a 3D confocal laser microscope (Olympus LEXT OLS 5000, Japan) was utilized to assess the surface roughness of the films, providing parameters such as Ra (arithmetic mean height of a line) and Sa (arithmetic mean height of the surface) for more comprehensive characterization of the surface topography.

To obtain comprehensive understanding of the nanostructure and composition of the NDC coatings, Raman spectroscopy was conducted using an Alpha 300R-confocal Raman Microscope (Witec, Germany). This technique offers crucial information on the bonding characteristics and the presence of specific chemical species within the film. The samples were illuminated with a 532 nm laser beam at 1 mW under cooling conditions to mitigate laser power thermal effects.

The mechanical properties of the film, particularly hardness and Young's modulus, were assessed through nanoindentation tests performed with a Fisher Instruments Company HM500 (Germany). To ensure the reliability and representativeness of the data, fifteen individual nanoindentation tests were conducted across the film surface. The film-substrate adhesion was also evaluated via a scratch test (Anton Paar RST^3), systematically applying a load range from 1 N to 60 N. This test used a diamond-tipped indenter, Rockwell N2–6266, with a load rate of 119.92 N/min and an applied traverse of 5 mm on the specimen. Further evaluation of adhesion strength and mechanical integrity was conducted via Rockwell D indentation tests under a maximum load of 100 kgf. This approach provided insights into the coatings' resistance to mechanical detachment or delamination from the WC − Co substrate, thereby assessing their suitability for demanding applications.

The tribological performance of the NDC-coated and uncoated WC − 6%Co pin substrates, was evaluated using a rotating pin-on-disc wear tester. The pin samples were evaluated against discs of Al_2O_3 counter-body. The tests were conducted under a vertical load of 2.94 N for 600 s, with a linear sliding velocity of 20 cm/s at room temperature. Wear behaviour on the film surfaces were then analysed using a 3D confocal laser microscope (LEXT OLS5000, Olympus, JP) to assess the durability of NDC coatings in terms of wear resistance. Furthermore, the wear rate of the films was determined using the Archard equation [40]: $k = \frac{V}{F \times L}$, where k represents the wear rate (mm^3/N·m), V is the wear volume (mm^3), F is the normal load (N), and L is the total sliding distance (m).

An electrochemical workstation (Model 660D, CH Instruments Inc.) equipped with a standard three-electrode system was used to investigate the corrosion behaviour of the WC − 6%Co before and after deposition of NDC films in a simulated corrosive environment. Tafel polarization tests were performed to assess the NDC coatings' resistance to corrosion. A saline solution (3.5 % NaCl) mimicked the corrosive conditions. The setup employed a working electrode (coated or noncoated WC − 6%Co substrate), a platinum counter electrode and a reference electrode (standard Ag/AgCl in 3 M KCl) for accurate measurements.

3. Results and discussion

3.1. Structural properties and surface morphology

NDC coatings were successfully deposited on WC − 6%Co substrates with a controlled thickness of 16 ± 1 µm at discharge energies of 3.6, 5.2, 7.0, and 9.0 J/pulse. Fig. 2 shows top-view and cross-sectional FESEM images with EDS, confirming the coatings' even coverage without peeling or delamination, unlike typical hard carbon coatings that delaminate due to non-etched Co's catalytic effects, which induce graphitization and weaken adhesion [41]. CAPD effectively limits these effects due to deposition at room substrate-temperature compared to CVD methods, which requires high substrate temperatures of nearly 800 °C for diamond growth [31,42].

Cross-sectional EDS profiling confirms that Co does not diffuse into the NDC films, with only an intense carbon peak detected. The non-

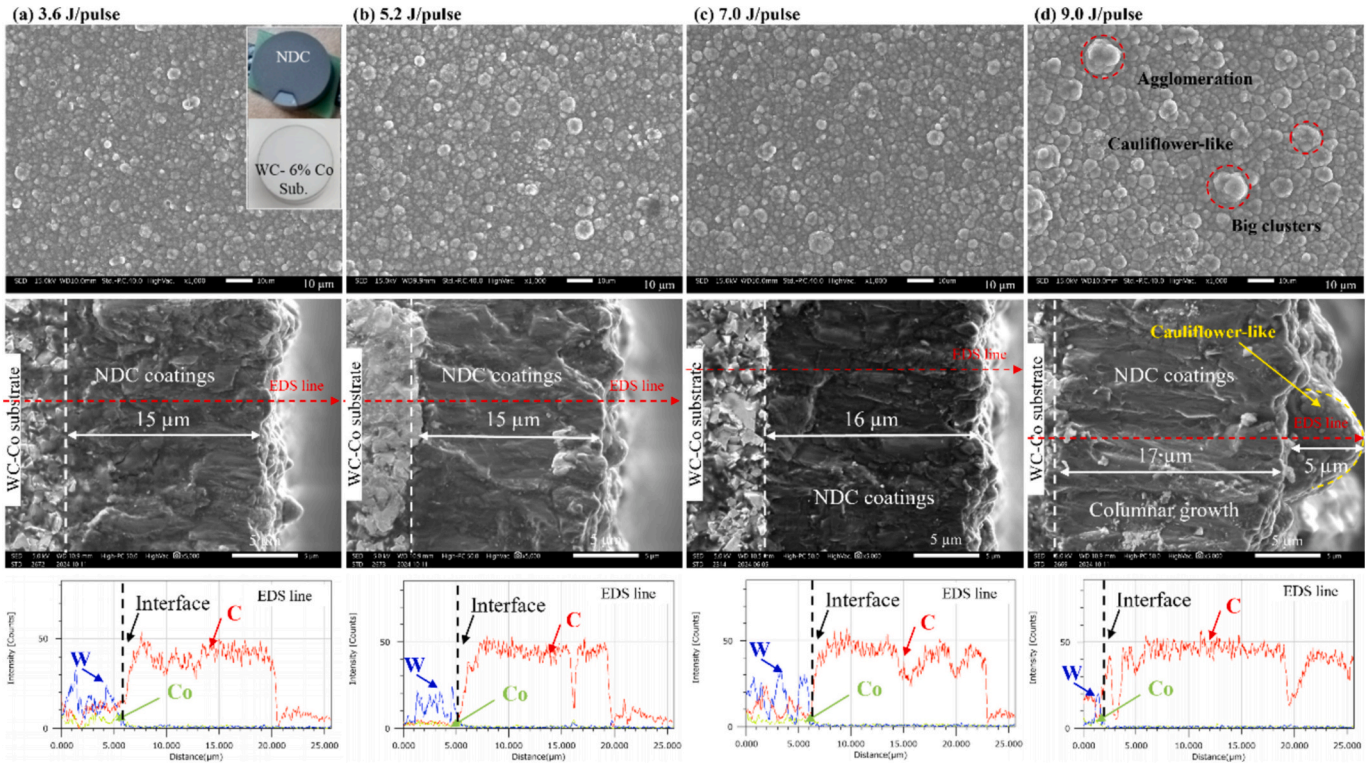

Fig. 2. Top-view FE-SEM images, cross-sectional microstructures, and cross-sectional EDS scans of NDC coatings deposited at discharge energies of (a) 3.6 J/pulse, (b) 5.2 J/pulse, (c) 7.0 J/pulse, and (d) 9.0 J/pulse.

uniform carbon profiles are attributed to the non-flatness of the cross-section, resulting from the natural fracture that occurs. This fracture prevents contamination, mitigates thermal impact, and reveals the true composition of the films. Secondary Ion Mass Spectrometry (SIMS) analysis supported the EDS findings, demonstrating the effectiveness of CAPD in controlling Co diffusion and reducing catalytic activity [43]. Consequently, a thick, stable 16 µm carbon film is achieved, free from delamination.

Surface morphology analysis reveals that the coatings exhibit a cauliflower-like structure, with a progressive increase in particle size proportional to the discharge energy. The presence of these particles is attributed to the ejection of un-fully ionized carbon phases, from the cathode during high-energy discharges (>7.0 J/pulse). The elevated arc energy input induces localized melting at the cathode spots, where intense plasma pressure expels molten material as macroparticles, driven by the significant intense heat generated at these spots, while the surrounding areas remain significantly cooler, near room temperature [44]. Upon reaching the substrate, these particles predominantly containing sp^2 bonds, act as nucleation sites [45], contributing to the observed size increase throughout the film cross-section from the substrate to the coating surface, as evident in SEM images (Figs. 2 and 13F). At 9.0 J/pulse, the coatings display larger cauliflower-like particles extending through the entire coating thickness, with a maximum dome height variation of 5 µm. This change in morphology may compromise coating properties, including reduced corrosion resistance, increased surface roughness, and elevated coefficient of friction.

Higher discharge energies promote both columnar growth and increased density in the coatings. During deposition, high-energy carbon ions generate a plasma enriched in C – C sp^3 bonds, as reported in previous studies on plasma properties [46]. Increased ion energy induces a denser, cauliflower-like structure, enhancing sp^3 bonding and mechanical properties.

However, as discharge energy increases, the plasma plume expands, with the projection area increasing from 27 to 44 cm^2 and the maximum diameter increasing from 59 cm to 80 cm. Consequently, the plasma moves closer to the substrate, while the target-substrate distance remains fixed throughout the experiments (Fig. 3). This results in a higher deposition rate and an increase in substrate temperature to approximately 100 °C, which enhances atomic mobility and promotes the agglomeration of cauliflower-like clusters, particularly at 9.0 J/pulse. These agglomerated particles contain non-fully ionized carbon species or sp^2 clusters within the coating. This shift in carbon bonding promotes a higher deposition rate, reduces internal stress, and increases the sp^2 fraction, ultimately diminishing the coating's hardness.

Raman analysis, as shown in Fig. 4, was employed to assess the structural and chemical composition of the NDC coatings, providing

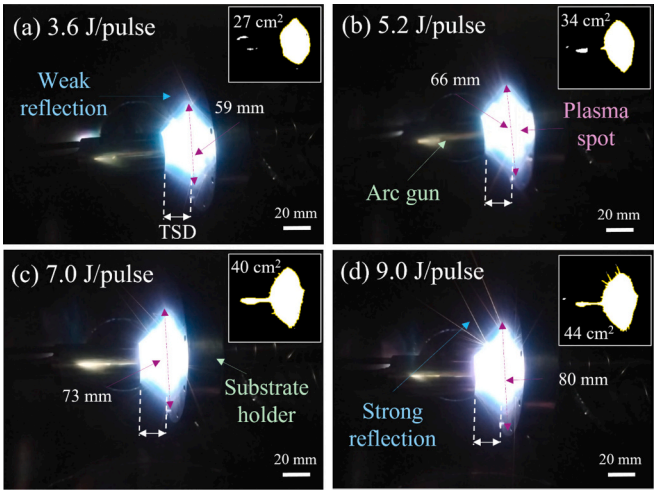

Fig. 3. Typical arc plasma plume images during NDC coating deposition at varying discharge energies: (a) 3.6 J/pulse, (b) 5.2 J/pulse, (c) 7.0 J/pulse, and (d) 9.0 J/pulse.

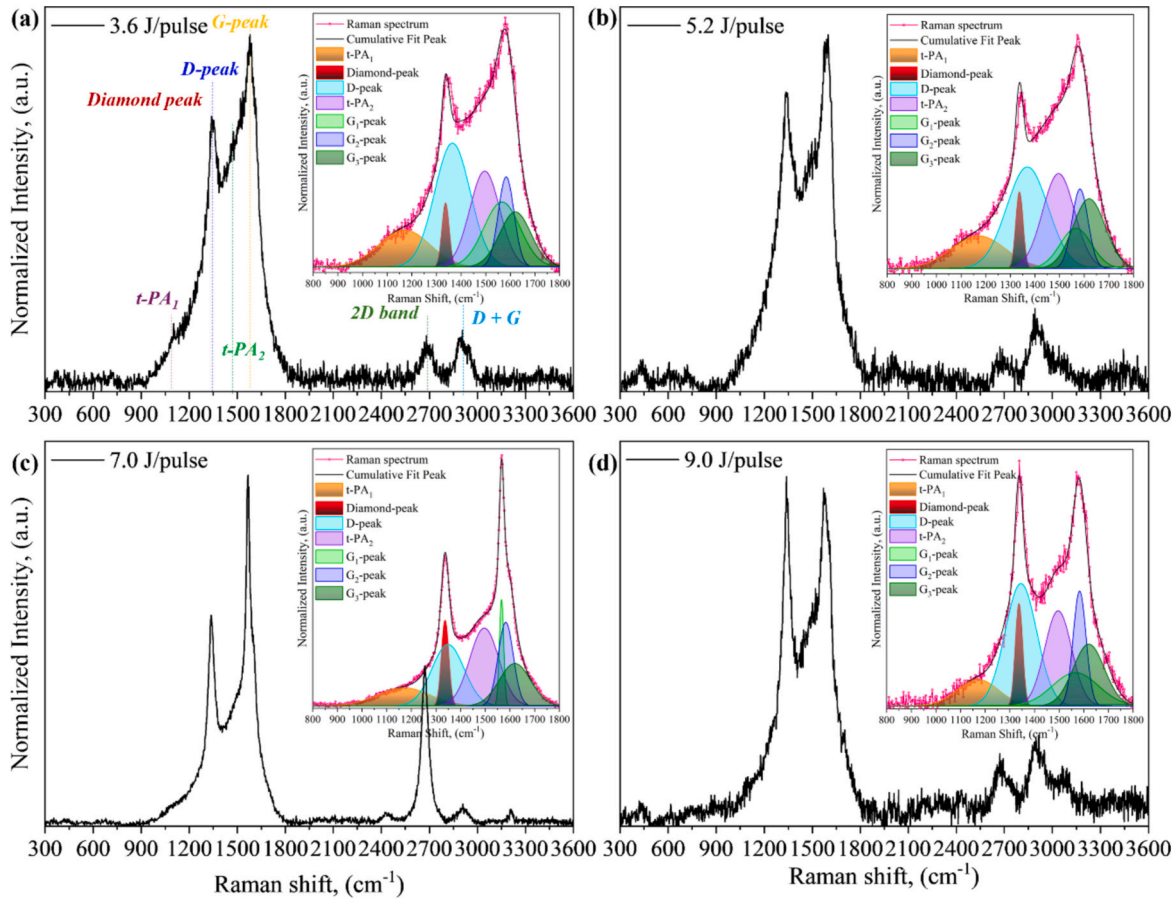

Fig. 4. Raman spectra of as-deposited nanodiamond composite films at varying discharge energies, highlighting characteristic peaks of the films' nanostructured composition.

insights into bonding configurations and carbon phases within the films. Raman bands were deconvoluted to elucidate the mechanisms influencing nanoindentation and friction properties across varying discharge energies in NDC deposition. Deconvolution of the broad band between 800 and 1800 cm^{-1} (Fig. 4 onset) revealed seven distinct peaks, indicating a nanostructured carbon material comprising nanodiamond crystallites (sp^3-bonded carbon) within an amorphous carbon (a-C) matrix. These nanodiamonds significantly contribute to the coating's hardness, while high-density grain boundaries (GBs), indicated by large areas of the t-PA_1 and t-PA_2 peaks, are primarily composed of sp^2 bonds, enhancing both growth and mechanical performance. Grain boundaries also act as dislocation sites, alleviating internal stress and promoting a low-friction transfer layer during tribological contact [47,48]. This assignment is consistent with previous studies comparing spectra from various carbon materials, including DLC, NDC, microcrystalline diamond (MCD), and nanocrystalline diamond (NCD) coatings, particularly focusing on the physical interpretation of the t-PA peaks [31,48,49].

A peak observed at 1337 cm^{-1} aligns with the typical diamond frequency at 1332 cm^{-1}, confirming nanodiamond integration, likely enabled by high-energy C^+ species generated in the CAPD plasma. Further evidence for the nanodiamond phase is provided by peaks at 1170 cm^{-1} and 1496 cm^{-1} (t-PA_1 and t-PA_2), attributed to *trans*-polyacetylene chains at grain boundaries [49–52], which support the nanoscale diamond phase's enhancement of tribo-mechanical properties.

The D-band at 1345 cm^{-1}, indicative of disordered graphite (A1g symmetry) [53], shows overlap with the diamond peak, corroborating previous studies on nanocrystalline diamond [54]. Additionally, the prominent G-band corresponds to the in-plane stretching vibrational mode (E2g) of carbon atoms in the hexagonal lattice, involving both ring and chain structures [45,55]. This band represents a mix of sp^3 diamond and sp^2 graphitic phases [55], both of which influence the coating's properties. It has been reported that the G-peak typically appears between 1510 and 1580 cm^{-1}, but can shift towards 1600 cm^{-1} when a high fraction of sp^3 chains is formed. The G-band is further split into three sub-peaks: G_1 at 1566 cm^{-1}, G_2 at 1583 cm^{-1}, and G_3 at 1610 cm^{-1}. The G_1 and G_2 peaks are linked to the sp^2 ring structure, and changes in these peaks reflect variations in this phase. On the other hand, the G_3 peak is associated with the sp^3 chain phase, enabling the monitoring of changes in this carbon structure.

The presence of the G_3 peak at 1610 cm^{-1} indicates that partial of sp^2 hybridized carbon atoms are transformed into sp^3 hybridized carbon atoms, forming sp^3-rich chains in a dense ta-C structure within the NDC film [45,55]. This transformation, likely influenced by the presence of nanodiamond crystallites, contributes to enhanced hardness and mechanical properties. The nanodiamond crystallites may serve as nucleation sites for the growth of ordered carbon, helping to reduce disorder and promote the formation of sp^3-bonded carbon phases.

A second broad band between 2000 and 3600 cm^{-1} represents second-order Raman scattering, reinforcing the presence of the nanodiamond phase. Within the 2500–3200 cm^{-1} range, a structured feature associated with disordered graphite includes a classic 2D band at 2680 cm^{-1}, a (D + G) band at 2900 cm^{-1}, and faint lines at 2260 and 2590 cm^{-1}, ascribed to second-order Raman scattering from t-PA modes [56]. These findings align with Raman data from CVD nanocrystalline diamond films [57], confirming a nanodiamond structure embedded within an amorphous carbon matrix in the NDC coatings.

In Raman spectroscopy of carbon nanomaterials, the area ratios of deconvoluted peaks are essential for evaluating the contributions from various bonding configurations [58]. These ratios offer insight into the

relative dominance of Raman signals linked to different carbon phases [48,59]. For instance, the ratio of the diamond peak (sp^3 phase) to the G-band (A_{dia}/A_G) reveals a notable trend: it increases from 0.09 at a discharge energy of 3.6 J/pulse, peaks at 0.2 at 7.0 J/pulse, and then declines to 0.16 at 9.0 J/pulse, as shown in Table 1. This progression aligns with variations in coating hardness, suggesting that hardness is directly influenced by the proportion of the existed diamond phase.

A similar trend appears in the ratios of the *trans*-polyacetylene peak to the G-band ($A_{t\text{-}PA}/A_G$) and the diamond peak to the D-band (A_{dia}/A_D), mirroring the pattern observed for A_{dia}/A_G. The lowest ratios occur at 3.6 J/pulse, with maximum values at 7.0 J/pulse, followed by a decline at 9.0 J/pulse. This pattern underscores the role of grain boundaries in contributing to the sp^2 content at diamond grain boundaries, further substantiating the presence of diamond crystallites within the coatings. Additionally, the integration of GBs in the NDC coatings mitigates compressive stress, enabling the deposition of films with significant thicknesses of 16 μm.

3.2. Mechanical characteristics

Fig. 5 presents the relationship between discharge energy and nanoindentation results for NDC coatings, with comparisons to the uncoated WC – 6 % Co substrate. The uncoated substrate shows an indentation hardness of 22 GPa and an elastic modulus of 527 GPa. For NDC coatings, hardness and modulus demonstrate a clear correlation with discharge energy. At 3.6 J/pulse, the coating achieves a hardness of 63.6 GPa and a Young's modulus of 672 GPa, which peak at 72.5 GPa and 694 GPa, respectively at 7 J/pulse.

This enhancement is attributed to the increased kinetic energy of ionized carbon (C^+) species at optimized discharge energies, promoting the formation of strong C – C sp^3 bonds. Furthermore, Raman spectroscopy analysis revealed the presence of the G_3 peak at 1610 cm^{-1}, indicative of a partial transformation of sp^2 to sp^3 hybridized carbon, contributing to the formation of sp^3-rich chains within the film. The presence of high-density grain boundaries within the NDC films further enhances structural integrity by acting as effective barriers to dislocation propagation, collectively contributing to the observed increase in hardness and elastic modulus.

The adhesion characteristics of the 16 μm-thick NDC coatings were assessed through both scratch testing and Rockwell hardness testing. The scratch test results, illustrated in Fig. 6, present the tangential force response as a function of progressively increasing normal load, providing a detailed evaluation of adhesion strength between the coating and substrate. Delamination, identified by a sharp rise in tangential force due to the release of elastic energy, determines the critical load (L_{cr}) marking coating adhesion [60,61]. Images of scratch tracks validate the exact delamination points, providing crucial information on adhesion strength. Findings show a positive correlation between discharge energy and adhesion strength, with critical load values increasing from 12.5 N to 42.5 N.

To further evaluate adhesion strength, Rockwell indentation testing was performed with a maximum load of 980 N (100 kgf), as illustrated in Fig. 7. Post-indentation evaluations, based on the classification criteria proposed by Vidakis et al. [63], identified different coating failure mechanisms, including cracking and delamination. Coatings produced

Table 1
Correlation between NDC film hardness and various area ratios (diamond peak to G peak (A_{dia}/A_G), diamond peak to D peak (A_{dia}/A_D), and *trans*-polyacetylene peak to G peak ($A_{t\text{-}PA}/A_G$)) across various discharge energies.

Discharge energy, (J/pulse)	Hardness, (GPa)	A_{dia}/A_G	A_{dia}/A_D	$A_{t\text{-}PA}/A_G$
3.6	63.6	0.09	0.11	0.86
5.2	67.0	0.12	0.13	1.00
7.0	72.5	0.20	0.32	1.05
9.0	65.0	0.16	0.19	0.75

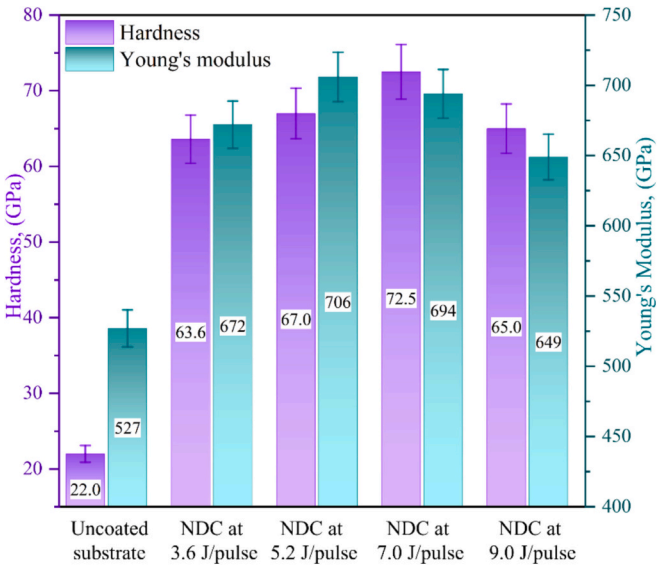

Fig. 5. Correlation of hardness and Young's modulus of NDC coatings deposited with varied discharge energies, compared to uncoated WC – 6 % Co.

at lower discharge energies (e.g., 3.6 J/pulse, Fig. 7a) displayed minor cracking and limited delamination in the vicinity of the indentation, reflecting satisfactory adhesion and toughness. Conversely, coatings fabricated at higher discharge energies (e.g., 7.0 J/pulse and 9.0 J/pulse) exhibited significantly enhanced adhesion and toughness, with negligible to no visible cracks or delamination.

These findings align with observations from scratch tests, which also indicated an enhancement in adhesion strength with increasing discharge energy. This improvement is primarily attributed to the closer proximity of the plasma plume at higher discharge energies, which elevates the substrate temperature to approximately 100 °C, promoting atomic mobility and reducing internal stresses. Raman analysis corroborates these observations, indicating an increased sp^2 fraction at higher discharge energies. This shift in bonding reduces compressive stress at the coating-substrate interface, contributing to overall adhesion improvement by relieving internal stresses [62].

3.3. Topographical and tribological characteristics

Surface roughness, a critical factor influencing frictional behaviour, was evaluated with surface roughness measured via a 3D laser confocal microscope, as shown in Fig. 8. NDC-coated pin-WC – 6%Co substrates exhibited surface roughness trends that aligned with those of flat samples, highlighting reproducibility across varied substrate geometries. With increasing discharge energy, the formation of cauliflower-like particles intensified, leading to elevated roughness values, including Ra and Sa, as shown in Fig. 8e. This pattern suggests efficient droplet removal and the generation of high-purity CAPD plasma at the optimal discharge energy of 7 J/pulse, which is also correlated with the coatings' peak hardness and sp^3 content. Notably, Sa values rose from 430 nm to 600 nm as discharge energy increased from 3.6 J/pulse to 9.0 J/pulse.

The NDC coatings also demonstrated increased surface roughness (Ra = 190–240 nm), likely attributable to the enlargement of sp^2 clusters within the film. This range closely corresponds with the substrate's initial roughness (Ra = 250–300 nm), suggesting that the substrate's surface texture significantly influences the final roughness characteristics of the coating.

The friction and wear characteristics of both uncoated and NDC-coated pin-substrates were evaluated against an Al_2O_3 counter-body under dry, open-air conditions, aligning with sustainability objectives by avoiding lubrication [64]. The uncoated substrates displayed a

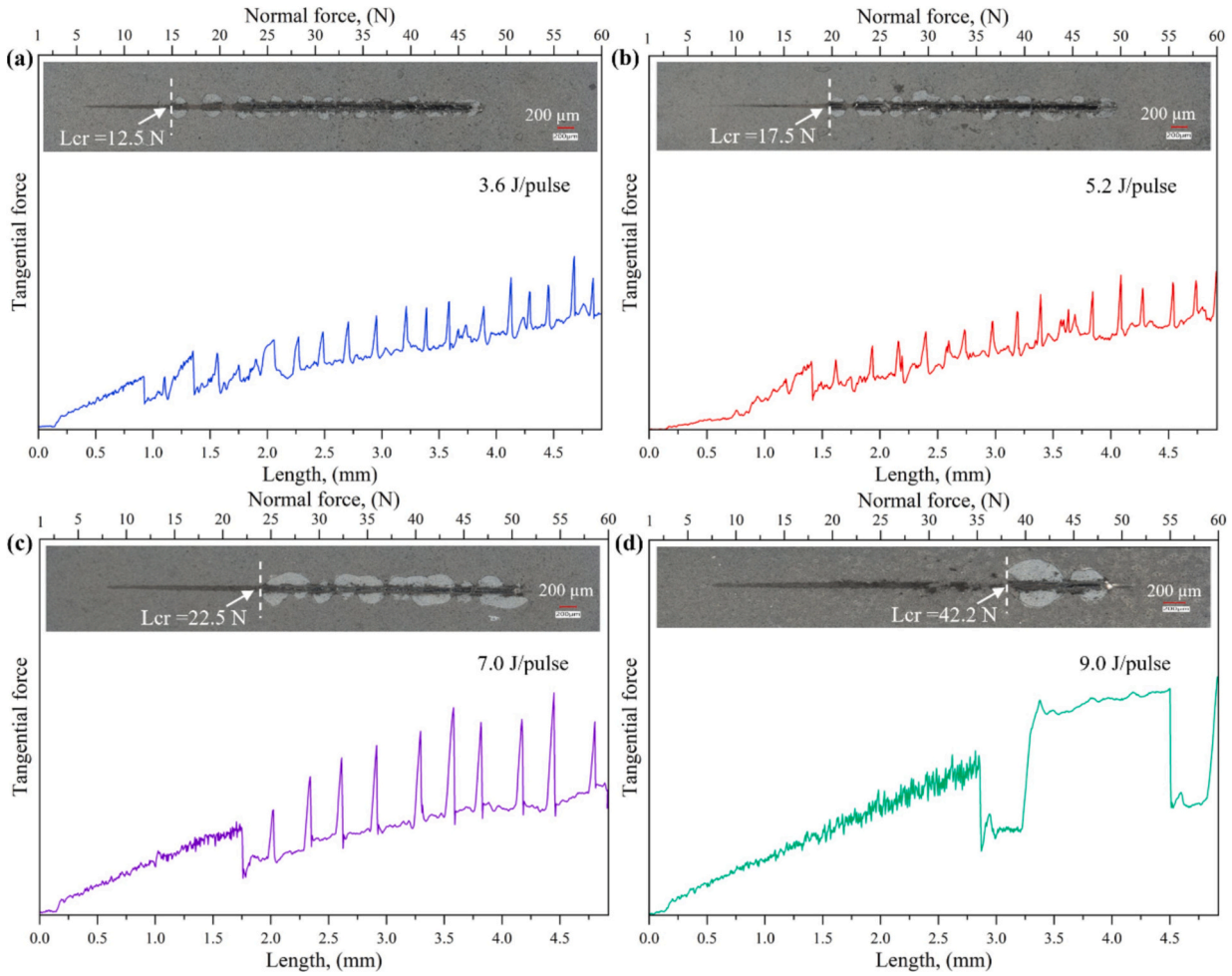

Fig. 6. Adhesion strength assessment: tangential force signals and corresponding optical image of the scratch track.

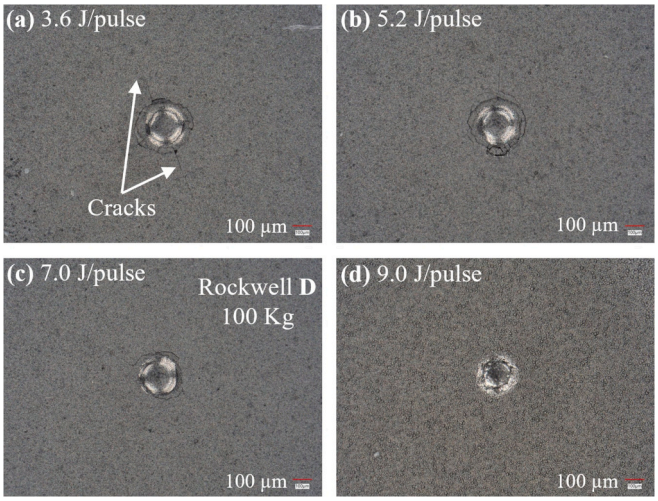

Fig. 7. Optical micrographs illustrating the crack and delamination morphology induced by Rockwell indentation on NDC coatings deposited at varying discharge energies: (a) 3.6, (b) 5.2, (c) 7.0, and (d) 9.0 J/pulse.

conventional COF profile, with an initial sharp increase followed by a gradual rise, attributed to abrasive interactions with Al_2O_3 and wear debris formation. This behaviour led to an extended transient phase before COF stabilization, as illustrated in Fig. 9a. The peak initial COF approached 1.0, indicative of high surface roughness and intensified abrasive contacts.

In contrast, NDC-coated samples exhibited a more structured COF profile, delineated into three distinct phases: break-in, transition, and steady-state. Initially, the COF was elevated (~0.25), likely due to surface asperities and prominent cauliflower-shaped particles present on the NDC coating. However, as these asperities worn down, the interface stabilized rapidly, achieving a steady-state COF within 5 s—a significantly faster stabilization relative to the uncoated substrates. Under dry sliding conditions, the NDC-coated samples achieved an average COF of 0.09, signifying an 7 factor reduction from the uncoated substrate's COF of 0.71, as illustrated in Fig. 9b.

As shown in Fig. 10, wear behaviour comparisons between uncoated and NDC-coated substrates, including 3D and 2D visualizations of worn areas, depth profiles, and wear tracks on the Al_2O_3 counter-body, reveal marked differences. Depth profile analysis indicates substantially shallower wear depths for NDC-coated samples relative to uncoated samples, correlating with the enhanced hardness of the coatings. The optimal discharge energy sample displayed the minimal wear depth of 1.78 µm compared to 5.7 µm for the uncoated sample. Wear resistance, assessed using the Archard equation [40], demonstrated nearly a tenfold increase in NDC-coated samples over uncoated substrates. The sample deposited at 7 J/pulse exhibited an exceptionally low wear rate of 1.88×10^{-7} $mm^3/N{\cdot}m$, achieving maximum wear resistance relative to the uncoated substrate (1.28×10^{-6} $mm^3/N{\cdot}m$), representing an improvement of approximately one order of magnitude. This superior wear resistance is further corroborated by the wear volume, which was significantly lower in NDC coatings (66,265 μm^3) compared to uncoated

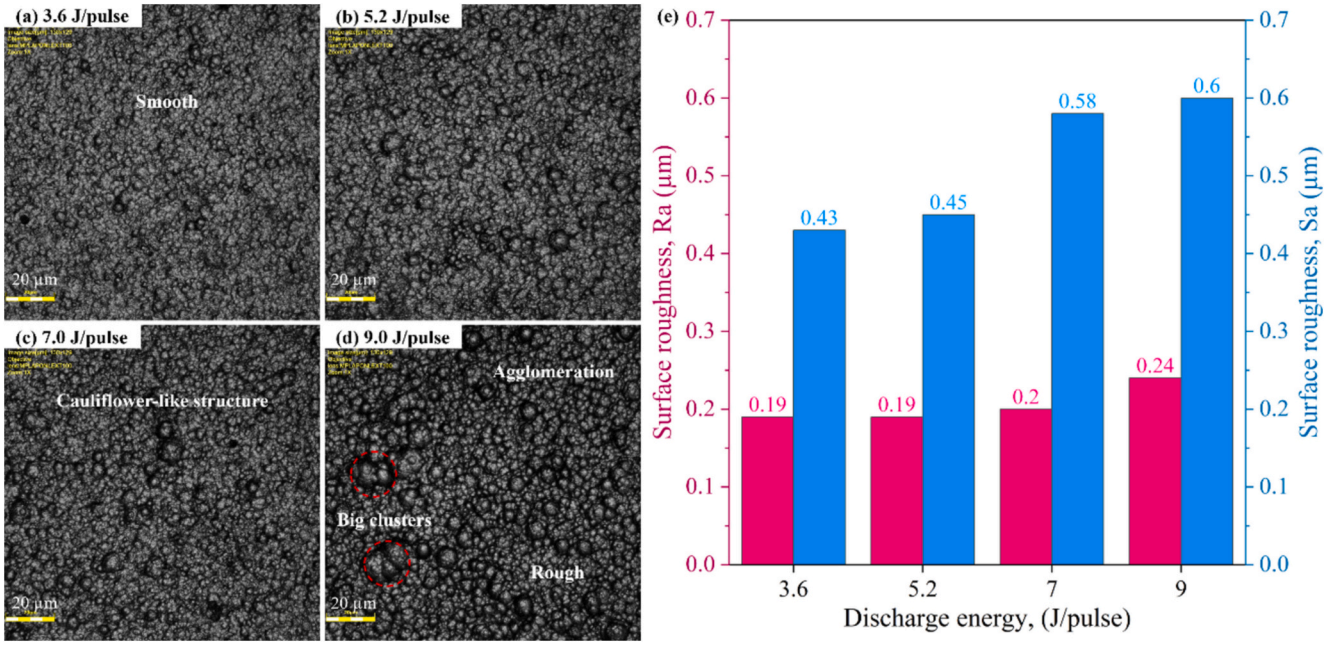

Fig. 8. 3D laser microscopy analysis of surface topography (Ra and Sa) of NDC-coated samples.

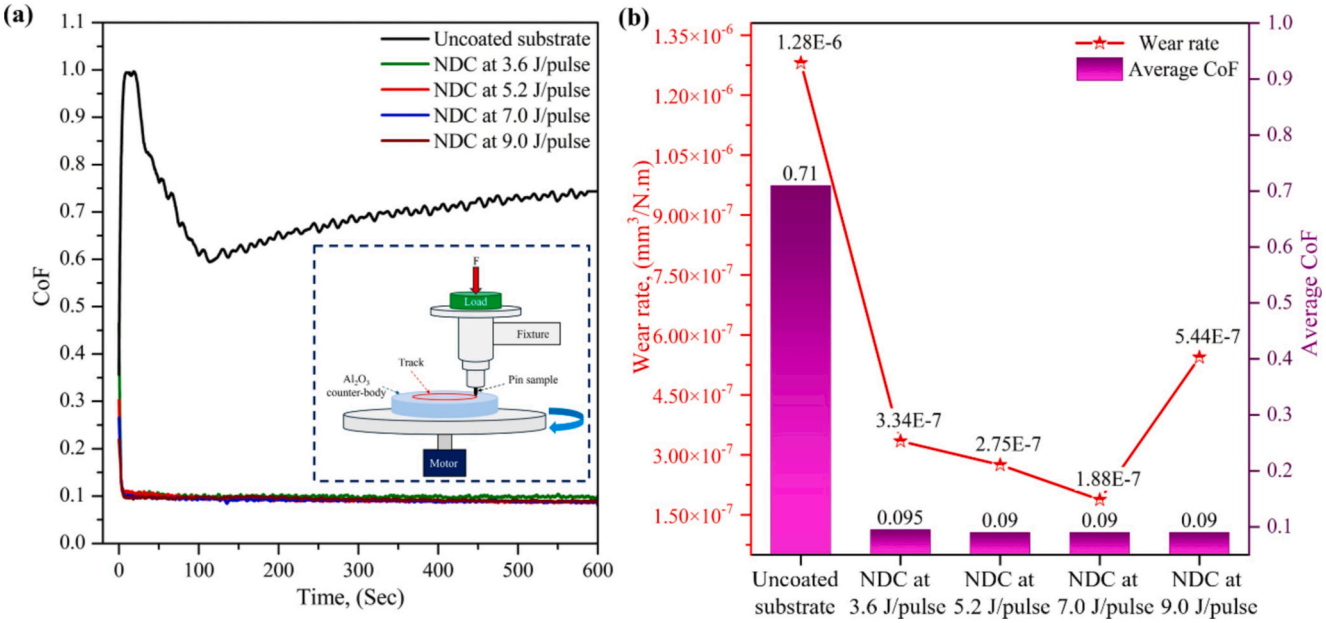

Fig. 9. COF vs. sliding time for uncoated and NDC-coated WC – 6%Co against Al_2O_3 counterpart in dry condition.

samples (451,838 μm^3). The relationship between coating hardness and wear depth, worn area on NDC samples, and wear track width on the Al_2O_3 counterpart confirms the role of hardness in enhancing wear resistance of NDC coatings.

The primary wear mechanism observed on tested surfaces was abrasive, as evidenced by the formation of furrows and debris on the worn areas of NDC-coated pin-substrates. Cauliflower-like particles on the NDC coatings fractured and detached under shear forces, producing small particles that acted as third bodies trapped between contact surfaces, forming grooves and contributing to wear. However, the surface interactions stabilized as testing continued, likely due to an increase in grain boundary content, aligning with the steady-state friction conditions observed in NDC films. Detailed 3D surface profiling further confirmed abrasive wear facilitated by the sharp asperities of both the NDC coating and the Al_2O_3 counter-body.

Several key mechanisms account for the superior tribological performance of NDC coatings. Initially, during the running-in phase, surface asperities smooth out, decreasing friction. Subsequently, a protective tribo-layer forms, aided by the rehybridization of sp^3 carbon atoms to sp^2 in addition to the sp^2 GBs, which act as a solid lubricant. This sp^2-enriched tribo-layer supports solid lubrication, lowering friction further and ensuring smoother mechanical performance. High wear resistance in NDC films can thus be attributed to their self-lubricating properties, high hardness, and the presence of grain boundaries within the nanocomposite matrix.

Meeting the established dry machining criteria (COF $\leq$ 0.1, wear rate $\leq 10^{-6}$ $mm^3/N{\cdot}m$) [65,66], NDC coatings effectively mitigate friction, prevent tool wear, and uphold dimensional and surface

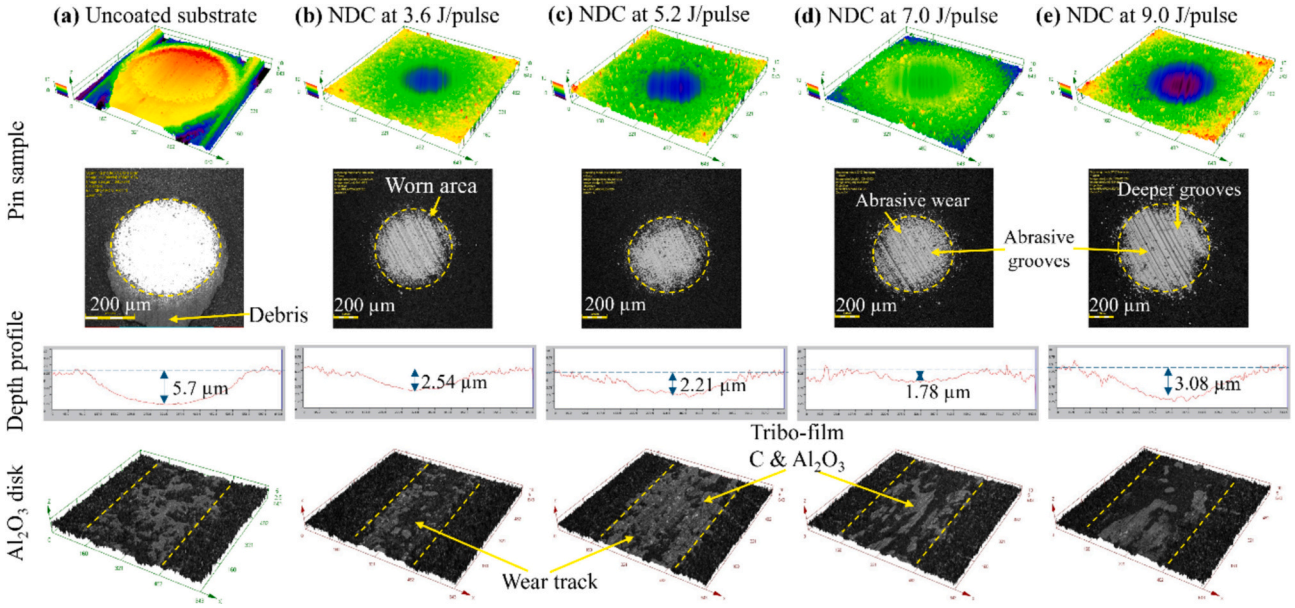

Fig. 10. Appearance of wear on uncoated and NDC-coated pin WC – 6%Co samples, along with wear appearance on alumina tracks post-friction.

integrity. These properties enhance tool longevity and reduce operational costs, aligning with sustainability objectives.

3.4. Corrosion resistance of NDC coatings

The potentiodynamic polarization (PDP) curves for both the WC – 6 % Co substrate and NDC-coated samples deposited at varying discharge energies, shown in Fig. 11, illustrate the corrosion resistance profiles of these materials. Notably, none of the samples exhibited fully passive behaviour, indicating the absence of a robust, self-repairing passive layer, such as oxides, to effectively mitigate corrosion [67,68]. This is evidenced by the continuous increase in corrosion activity, as indicated by rising current levels, with increasing potential. The anodic polarization of the WC – 6 % Co substrate reflects active dissolution, underscoring the substrate's inherently low corrosion resistance in a 3.5 wt% NaCl solution. This sample displayed the lowest potential energy (E_{corr}), measured at −336 mV, as summarized in Table 2. The NDC coatings' corrosion potential increased with discharge energy, peaking at −206 mV for the sample deposited at 7 J/pulse, before declining to −277 mV for the coating deposited at 9 J/pulse. A lower corrosion potential (more negative) signifies a higher tendency for the material to undergo corrosion, and vice versa, indicating the greater corrosion resistance of the NDC-coated WC – 6%Co substrate (−206 mV) compared with the other samples.

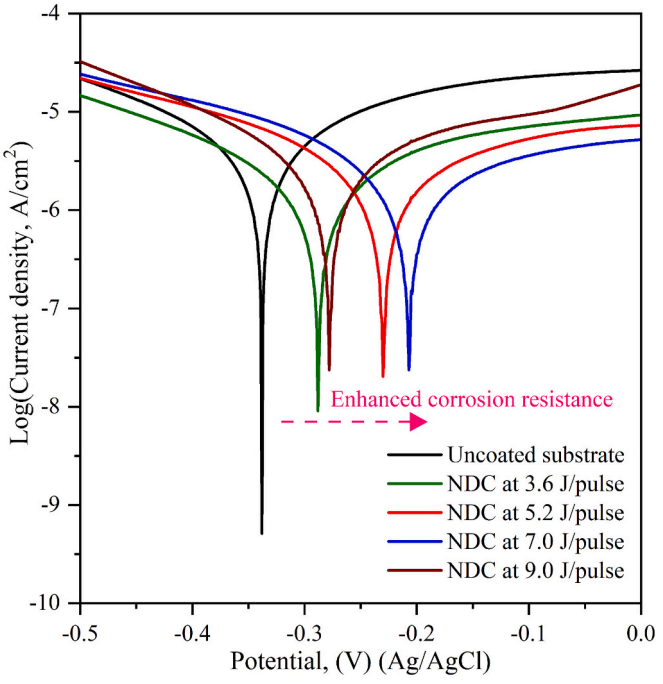

Fig. 11. Potentiodynamic polarization curves comparing corrosion resistance of NDC-coated and uncoated WC – 6%Co substrates.

The NDC-coated sample prepared at 7.0 J/pulse exhibited the lowest corrosion current density (I_{corr} of 1.971×10^{-3} mA/cm^2), significantly reducing corrosion activity compared to the uncoated substrate ($I_{corr} = 4.976 \times 10^{-3}$ mA/cm^2). This improvement corresponds to a decrease in the annual corrosion rate from 1.297 to 0.5136 mil/year. These results indicate that the NDC coating offers enhanced protection in highly corrosive environments (3.5 wt% NaCl saline solution) by significantly improving the substrate's corrosion resistance. Furthermore, the findings highlight that NDC coatings deposited at 7.0 J/pulse exhibit partial surface passivation, significantly enhancing the corrosion resistance of WC–6%Co substrates, demonstrating the potential of these coatings for reliable application in harsh and corrosive environments.

FESEM micrographs and EDS analysis of the WC – 6 % Co substrate surface, before and after exposure to the NaCl solution, are presented in Fig. 12. Clear signs of localized corrosion are visible in the cobalt binder, confirming galvanic corrosion. These observations align with the active dissolution indicated by the PDP curves. EDS analysis of the uncoated WC – 6 % Co sample (Fig. 12B) supports these findings, revealing a reduction in cobalt content post-corrosion, with levels decreasing from 6.40 at.% to 4.24 at.%, indicating substantial binder phase dissolution. This dissolution arises from the electrochemical potential difference

Table 2
Comparison between the uncoated WC – 6%Co substrate and NDC coatings.

Sample	E_{corr}, (mV)	Corr. rate, (mil/year)	I_{corr}, (mA/cm^2)
WC-6 % Co substrate	−336	1.297	4.976E-3
NDC at 3.6 J/pulse	−287	0.6533	2.507E-3
NDC at 5.2 J/pulse	−230	0.6232	2.392E-3
NDC at 7.0 J/pulse	−206	0.5136	1.971E-3
NDC at 9.0 J/pulse	−277	0.8379	3.631E-3

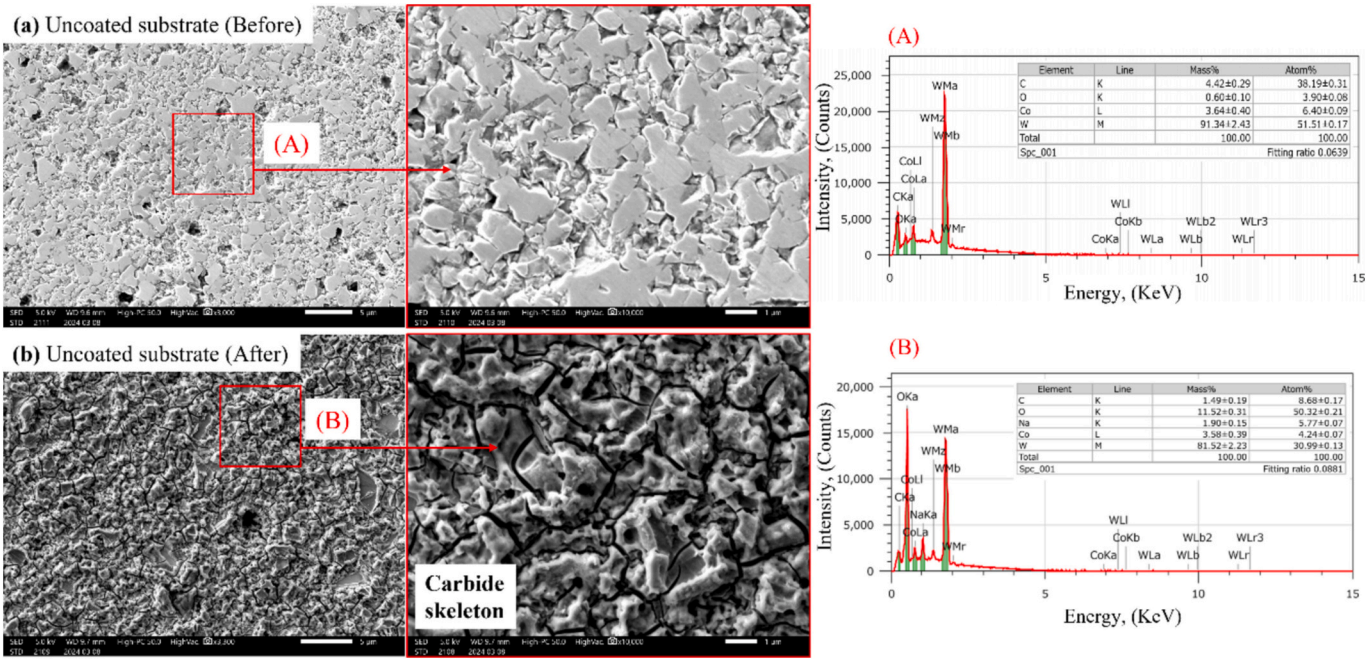

Fig. 12. Surface FESEM micrographs and EDS analysis of uncoated WC − 6 % Co samples: (a) prior to corrosion testing, and (b) following exposure to 3.5 wt% NaCl solution.

between the cobalt binder and WC phase, which accelerates galvanic corrosion in acidic environments [9]. Thus, the WC − 6 % Co substrate displays a clear susceptibility to corrosion, as evidenced by localized degradation of the cobalt binder.

Surface micrographs of the NDC-coated samples following corrosion tests, as presented in Fig. 13a–d, reveal minimal damage to the coating

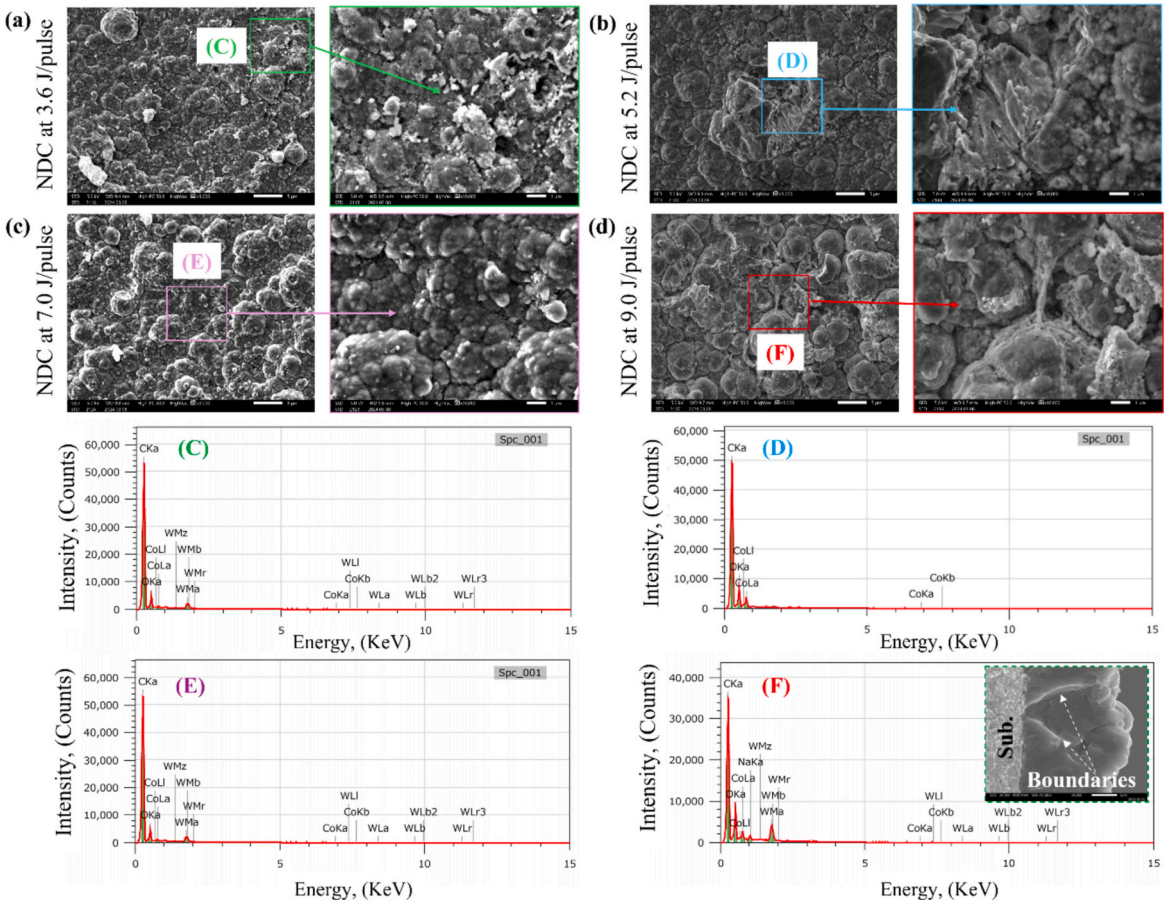

Fig. 13. Surface FE-SEM micrographs and EDS results of NDC coatings deposited at different discharge energies after corrosion testing in 3.5 wt% NaCl solution.

deposited at 7.0 J/pulse, underscoring its superior corrosion resistance attributed to its dense structure. FE-SEM micrographs captured at various magnifications further illustrate the resilience of this coating, indicating negligible damage post-testing. In contrast, other NDC coatings displayed varying levels of degradation, with the coatings deposited at 9.0 J/pulse exhibiting the most significant deterioration. This severe damage is primarily attributed to the presence of larger cauliflower-like particle sizes, which enable the infiltration of the NaCl solution through interparticle boundaries, facilitating penetration through the entire thickness of the coating. The onset of Fig. 13F delineates the boundaries of the detached large cauliflower-like particles, which facilitate the substrate corrosion rate.

To assess corrosion resistance more comprehensively, EDS analysis was conducted on specific regions (Fig. 13C-F), revealing prominent carbon peaks along with minor peaks potentially indicative of surface oxidation. Notably, no delamination or significant cobalt dissolution was observed, highlighting the protective capability of the NDC coatings, which were applied via the environmentally favourable CAPD technique. The superior corrosion resistance of the NDC coatings, particularly those deposited at the optimal discharge energy of 7 J/pulse, can be attributed to their dense nanostructure and enhanced mechanical properties, underscoring their effectiveness in protecting WC − 6 % Co substrates in corrosive conditions.

Table 3
Potential of sustainable NDC coatings on WC − Co substrates in comparison with different coatings (CAPD vs well-established technique).

Coating type	Deposition technique	Thickness, (μm)	Deposition parameters		Mechanical properties		Tribological characteristics				Corrosion resistance	
			Deposition rate, (μm/h)	Substrate temperature, (°C)	Hardness, (GPa)	Adhesion strength, (N)	Friction load, (N)	Counter-body	Average COF	Specific wear rate, (mm^3/N·m)	Corrosive media	Ecorr, (mV)
MCD	HFCVD [60]	~6.5	~0.72 [69]	800–850	~58	42	–	–	–	–	–	–
NCD					~40	20	–	–	–	–	–	–
MCD	HFCVD [70]	10	0.5	800	~80	–	3	Al_2O_3	0.182	8.41×10^{-8}	–	–
ta-C	Vacuum cathodic arc [71]	0.383–0.5	0.76–1	–	47.4–58.7	–	5	Steel ball (GCr15)	0.14–0.18	$1.81–2.2 \times 10^{-7}$	–	–
TiN	Cathodic arc-evaporation [72]	2	–	500	2240 $HV_{0.5}$	–	10	SiC	0.66	4×10^{-7}	–	–
TiAlN		1.2	–		3250 $HV_{0.5}$	–			0.70	2×10^{-7}	–	–
AlTiN		1.3	–		3140 $HV_{0.5}$	–			0.77	45×10^{-7}	–	–
CrAlN		1.8	–		3160 $HV_{0.5}$	–			0.73	20×10^{-7}	–	–
TiN	CAE-PVD method [15]	–	–	–	–	–	–	–	–	–	3.5 %	−310
TiCN		–	–	–	–	–	–	–	–	–	NaCl	−334
TiAlN		–	–	–	–	–	–	–	–	–	solution	−322
a-C	Electron cyclotron resonance (ECR) ion irradiation [73]	0.1	–	Below 50	16.2	15.99	3	304 stainless steel ball	0.111-o.145	–	–	–
TiN/TiCN/TiCN/TiC/TiN	CVD [1]	15.7	–	1000–1030	–	–	5	WC-6Co pin	~ 1	–	3.5 wt% NaCl medium	−390
TiN/TiCN/TiCN/TiC/Al_2O_3		9.3	–		–	–			0.5–1.1	–		−360
NDC (E = 3.6 J/pulse)	CAPD (current work)	16 ± 1	3.2	No external heating	63.6	12.5	2.94	Al_2O_3	0.095	3.34×10^{-7}	Saline solution (3.5 % NaCl)	−287
NDC (E = 5.2 J/pulse)			4.2		67.0	17.5	2.94		0.09	2.75×10^{-7}		−230
NDC (E = 7.0 J/pulse)			4.9		72.5	22.5	2.94		0.09	1.88×10^{-7}		−206
NDC (E = 9.0 J/pulse)			5.7		65.0	42.2	2.94		0.09	5.44×10^{-7}		−277

MCD: Microcrystalline Diamond; NCD: Nanocrystalline Diamond; NDC: Nanodiamond Composite; ta-C: Tetrahedral amorphous Carbon; CrAlN: Chromium Aluminum Nitride; TiAlN: Titanium Aluminum Nitride; TiN: Titanium Nitride; TiCN: Titanium Carbonitride; E: Discharging Energy.

3.5. Comparison between NDC coatings and other coatings for cutting tools applications

This section investigates the potential of NDC coatings to surpass the performance of established cutting tool coatings, including microcrystalline diamond (MCD), nanocrystalline diamond (NCD), and transition metal nitrides (TiN, TiAlN, CrAlN). Comparative data presented in Table 3 highlights the distinct advantages of NDC coatings in terms of mechanical properties, tribological performance, and corrosion resistance.

The NDC coating, deposited via the CAPD method at optimal discharge energy of 7.0 J/pulse, achieved thicknesses of 16 ± 1 μm with deposition rates of 4.9 μm/h, demonstrating higher deposition efficiency than MCD coatings deposited via HFCVD, which typically reach 10 μm thickness at slower rates (0.5–0.72 μm/h). Additionally, NDC coatings grow without external substrate heating or chemical etching of Co from the substrate surface, simplifying the deposition process.

NDC coatings exhibit exceptional hardness (up to 72.5 GPa), competing with MCD coatings (58–80 GPa) and outperforming transition metal nitrides such as TiAlN (approximately 31.4 GPa) and CrAlN (approximately 30.9 GPa). In terms of adhesion strength, NDC coatings achieved critical loads of up to 22.5 N, which exceeds values reported for directly deposited MCD coatings without Co etching. However, the adhesion strength achieved at the highest hardness level requires further enhancement to meet the demands of dry machining conditions.

NDC coatings also exhibit superior tribological performance, with cCOF as low as 0.09, representing an 86 % improvement compared to TiN (0.66) and a 24–38 % improvement compared to ta-C (0.111–0.145). Moreover, NDC coatings demonstrate significantly lower wear rates (down to 1.88×10^{-7} $mm^3/N{\cdot}m$) compared to TiN (4×10^{-7} $mm^3/N{\cdot}m$) and ta-C ($1.81–2.2 \times 10^{-7}$ $mm^3/N{\cdot}m$).

Corrosion resistance data further emphasize the advantages of NDC coatings. With a corrosion potential (E_{corr}) of −206 mV in saline solution, NDC coatings outperform TiN (−310 mV) and TiCN (−334 mV) coatings, contributing to prolonged durability in aggressive environments.

These combined properties, including exceptional hardness, reasonable adhesion, low friction, and wear resistance, coupled with good corrosion resistance, underscore the potential of NDC coatings as a promising alternative to conventional coatings for advancing cutting tool technology.

3.6. Sustainability assessment

Modern manufacturing emphasizes the adoption of eco-friendly practices, including the implementation of dry cutting processes that eliminate the use of coolant fluids [74]. Dry cutting offers significant environmental and economic benefits by minimizing waste generation and reducing operational costs by up to 20 % while maintaining high machining precision [75]. Coatings designed for dry cutting applications must function effectively as heat barriers, mitigating friction and wear. While existing coatings offer some benefits, further research is necessary to fully optimize their performance for improved sustainability in machining processes. Sustainability assessments employing the "3-E" framework (Energy, Economic, Environment) underscore the potential of NDC coatings as a viable solution for advancing cutting tool technologies.

3.6.1. Energy analysis

The energy efficiency of CAPD in NDC coating deposition offers a clear advantage over methods such as CVD. By utilizing arc plasma to generate energetic carbon species from a solid target, CAPD eliminates the need for external heating, resulting in a more energy-efficient process. As discharge energy increases from 3.6 to 9.0 J/pulse, the substrate temperature rises from room temperature to a maximum of 100 °C, which is significantly lower than the 800 °C required for CVD diamond growth due to its low deposition rate [76]. This controlled temperature increase in CAPD preserves the mechanical integrity of WC − 6%Co substrates, which are vital for high-stress applications like cutting tools.

CAPD's energy efficiency is primarily attributed to the arc plasma gun, which consumes between 60.8 and 96.6 kWh, accounting for 77.5–87.7 % of total energy usage. This is calculated based on discharge energy and deposition time (Eqs. (1)–(3)). The energy consumption in CAPD can be categorized into three components (Fig. 14): arc plasma energy (the major contributor), pumping energy (10.6 to 16.6 kWh), and minimal post-deposition cooling energy (1–3 kWh). By minimizing unnecessary energy expenditure, CAPD reduces operational costs and complexity compared to CVD, which requires additional external heating, gases, and cooling systems.

$$P_T = P_{Arc} + P_{Pumping} + P_{Cooling} \quad (1)$$

$$P_{Arc} = p_{dicharge} \times t_{deposition} \quad (2)$$

$$P_{Pumping} = P_{TMP} + P_{RP} \quad (3)$$

where, $P_{discharge}$ is the coating energy consumption (KW), $t_{deposition}$ is deposition time (h), and the components like pumps $(P_{Pumping})$, heating (0), etching (0), and cooling $(P_{Cooling})$ (kWh).

3.6.2. Environmental impact

Environmental sustainability is enhanced by CAPD's operating conditions, which circumvent the use of harsh chemicals and hazardous gases typically required in CVD processes. CAPD achieves a high deposition rate, ranging from 3.2 to 5.7 μm/h as discharge energy increases (Fig. 14), offering an efficient coating solution without compromising environmental safety. By eliminating the need for chemical etching of Co and the use of toxic deposition gases, CAPD contributes to a safer work environment, reduces local pollution, and mitigates health risks for workers. These factors underscore CAPD's potential as a cleaner and more environmentally responsible coating technique.

3.6.3. Cost analysis

The economic feasibility of NDC coatings is significantly influenced by the energy efficiency and simplified design of the CAPD process. High deposition rates (3.2 to 5.7 μm/h) achieved in CAPD, significantly exceeding those observed in CVD processes (0.5 to 2 μm/h) [77], translate to shorter processing times and increased throughput, enhancing production efficiency and reducing overall manufacturing costs.

The CAPD system features a simplified design, incorporating a vacuum system employing mechanical and turbomolecular pumps, a

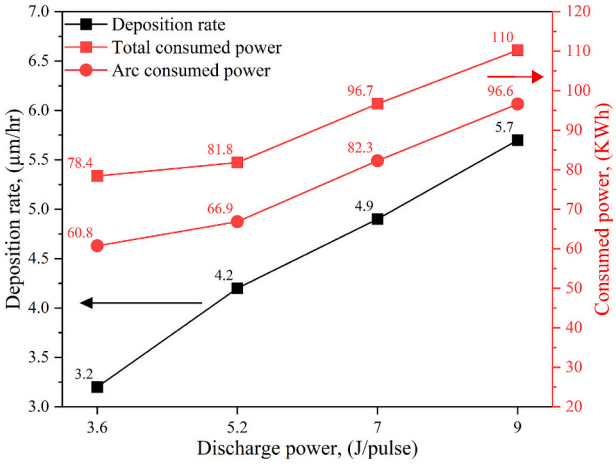

Fig. 14. Correlation between deposition rate, arc gun power consumption, and total power consumption as a function of discharge energy variations.

stainless-steel deposition chamber (304-grade), and a plasma arc gun. This streamlined setup significantly reduces capital equipment costs compared to complex CVD systems that often require expensive microwave or hot filament plasma sources, elaborate gas handling systems, and sophisticated temperature control mechanisms.

Furthermore, the operational costs of CAPD are minimized due to the elimination of external heating systems, the use of a simple and readily available graphite target, and the reduced reliance on expensive gases. The simplified system design also contributes to lower maintenance costs and reduced environmental impact by minimizing the generation of hazardous waste and the consumption of resources.

Table 4 provides a comparative analysis of NDC coatings fabricated by the environmentally friendly CAPD method with other established coating techniques, including HF-CVD for MCD, arc ion plating for ta-C, and cathodic arc evaporation for TiCN. The table outlines the capital costs, substrate materials, pre-treatment processes, coating sources, deposition times, temperatures, layer thicknesses, hardness values, total energy consumption, and estimated cost per micrometre of coating thickness for each case study.

In this case only the equipment needed for the sole purpose of coating ten substrates at a time using one chamber is considered. The total cost C_{TOT} is given in Eq. (4).

$$C_{TOT} = C_{OP} + C_L + C_{EQ} \quad (4)$$

$$C_{OP} = C_{ELEC} + C_{MAT} \quad (5)$$

$$C_{EQ} = C_M + C_A \quad (6)$$

where, C_{OP} is the operating cost; C_L is the labor cost; C_{EQ} is the equipment cost; C_{ELEC} is the cost of electricity; C_{MAT} is the cost of the materials used; C_M is the maintenance cost and C_A is the cost of annuity.

The annuity and maintenance costs are based on several assumptions, including a yearly maintenance cost of 2 % of the equipment investment [78]. The equipment is presumed to operate continuously for two shifts per day (16 h) for 300 days a year, with an expected lifespan of 15 years. Prices sourced from different currencies were adjusted for inflation and converted to US dollars using the exchange rate of 1 USD = 149.22 JPY.

The estimated cost per micrometre of NDC coatings produced by CAPD is expected to be competitive with, and in some cases, lower than that of other established coating techniques. This, combined with the high deposition rates, reduced energy consumption, and simplified system design, demonstrates the strong economic viability of the CAPD process for the industrial-scale production of high-performance NDC coatings for cutting tool applications.

3.6.4. SWOT analysis

A SWOT analysis, depicted in Fig. 15, reveals the significant potential of NDC coatings within the context of sustainable manufacturing. Strengths of NDC coatings include enhanced durability and performance, leading to extended tool life and reduced operational costs. The CAPD technique employed for their deposition offers advantages such as simplicity, cost-effectiveness, and reduced environmental impact compared to conventional methods. Weaknesses include potential limitations in scalability and the need for further research to optimize deposition parameters for various applications.

Opportunities for NDC coatings are significant, driven by the growing demand for environmentally friendly manufacturing processes that align with global sustainability goals. The ability of NDC coatings to minimize environmental impact while improving tool performance positions them to be considered in the market. However, threats include competition from alternative coating technologies and the need for broader industry acceptance and implementation of this emerging technology.

This SWOT analysis underscores the considerable potential of NDC coatings produced via the CAPD technique, particularly in hard coating applications. It highlights the need for continued research and development to address potential weaknesses and capitalize on the identified opportunities, ultimately paving the way for the widespread adoption of NDC coatings in sustainable manufacturing practices.

4. Conclusion

This research aimed to deposit and optimize sustainable thick-superhard NDC coatings on WC − 6%Co hard metal using the eco-friendly CAPD technique, addressing the critical challenge of enhancing cutting tool performance such as limited wear and corrosion resistance while minimizing environmental impacts associated with traditional coating methods. Unlike conventional techniques that often involve harmful chemicals and significant energy consumption, the CAPD approach employed in this study is characterized by its low environmental footprint, promoting sustainability throughout the coating process. The study demonstrated that varying discharge energies (3.6, 5.2, 7.0, and 9.0 J/pulse) significantly affected the deposition rates, which increased by 78 % from 3.2 to 5.7 μm/h, achieving coating thicknesses of up to 16 μm. The hardness peaked at 72.5 GPa at 7.0 J/pulse, with adhesion strength rising by 240 % to 42.5 N due to internal stress release at the coatings-substrate interface. Wear resistance was markedly improved, with wear rates decreasing from 1.28E-6 to 1.88E-7 mm^3/N·m at 7.0 J/pulse, representing an order of magnitude enhancement over uncoated substrates. This improvement correlates

Table 4
Comparison between NDC coatings fabricated by eco-friendly CAPD and well-established CVD diamond coatings fabricated by HF-CVD, ta-C coating fabricated by arc ion plating, and TiCN fabricated by cathodic arc evaporation.

Case study	HF-CVD [79]	AIP [80]	Vacuum cathodic arc [71]	CAE [81]	CAPD (current work)
Coating name	CVD diamond	ta-C	ta-C	TiCN	NDC
Capital cost	–	–	–	–	~160,000 $
Substrate	Cemented carbide (WC − Co)	Cemented carbide (WC − Co)	Cemented carbide (WC − Co)	Cemented carbide (WC − Co)	Cemented carbide (WC − Co)
Pre-treatment	Roughening + etching of Co + seeding	Polishing	Polishing + Etching + Cr interlayer	Etching	Roughening
Coating sources	Hydrogen (H_2) and methane (CH_4)	Pure graphite target	Pure graphite targets and Cr target	Ti target, Ar, C_2H_2, and N_2	Pure graphite target
Deposition time	13 h	30 min	10 min Cr interlayer + 30 min ta-C	3 h 27 min	3 h 26 min
Deposition temperature	800–850 °C	~150 °C	–	~450 °C	Room temperature
Layer thickness	3.5 μm	0.15 μm	0.16–0.172 μm Cr + 0.383–0.5 μm ta-C	2.5 μm	16 μm
Hardness, (GPa)	80.2	60	47.4–58.7	–	72.5
Total energy consumption	–	–	–	101 kWh	96.7 kWh
Cost ($/μm)	–	–	–	–	0.75 $ = 12.27 JPY

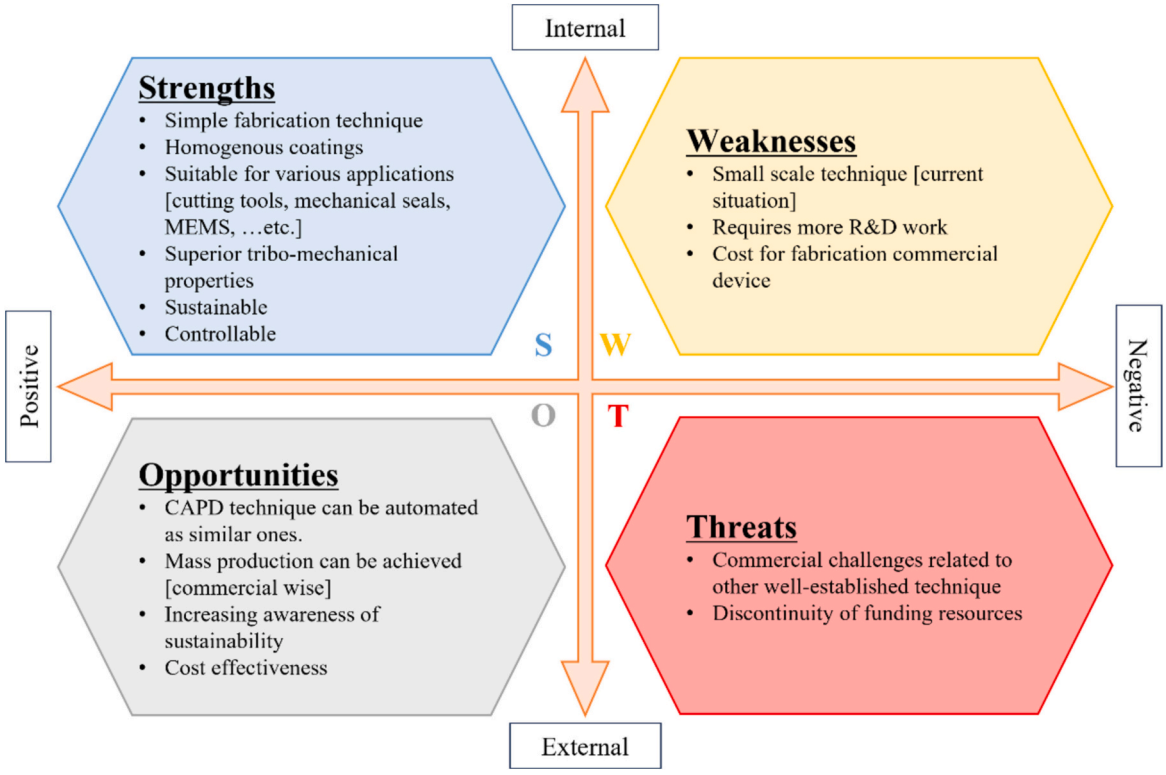

Fig. 15. SWOT analysis quadrant map for sustainable NDC coatings fabricated by eco-friendly CAPD technique towards advanced cutting tool applications.

with the coatings' hardness and dense structure, which may effectively withstand mechanical stresses during cutting operations. Additionally, the NDC coatings maintained a COF of approximately 0.09, representing a sevenfold reduction compared to the uncoated WC – 6%Co substrate (0.71), attributed to the presence of an sp^2-rich transfer layer enhancing sliding properties. Corrosion resistance was also improved, achieving a corrosion rate of 0.5136 mil/year at 7.0 J/pulse, reflecting a 60.4 % enhancement over uncoated substrates, although resistance diminished at 9.0 J/pulse due to the increasing size of cauliflower-like particles allowing solution penetration. The effectiveness of NDC coatings deposited via CAPD was assessed as a sustainable and viable solution for enhancing the longevity and performance of WC – 6%Co hard metal for cutting tools application.

CRediT authorship contribution statement

Alaaeldin Mohamed: Writing – review & editing, Supervision. **Ahmed A. Farghali:** Writing – review & editing, Supervision. **Ahmed M.E. Khalil:** Writing – review & editing, Methodology. **Mohamed Sh. Abdel-Wahab:** Writing – review & editing, Methodology. **Wael Z. Tawfik:** Writing – review & editing, Methodology. **Ayman Ali Saeed:** Methodology, Investigation. **Mohamed Ragab Diab:** Writing – original draft, visualisation, Methodology. **Koki Murasawa:** Resources, Methodology, Investigation. **Hiroshi Naragino:** Resources, Methodology. **Tsuyoshi Yoshitake:** Writing – review & editing, Resources, Methodology, Funding acquisition. **Mohamed Egiza:** Writing – review & editing, Writing – original draft, Project administration, Methodology, Conceptualization.

Declaration of competing interest

The authors declare that they have no known competing financial interests or personal relationships that could have appeared to influence the work reported in this paper.

Acknowledgements

This research was partially funded by The Osawa Scientific Studies Grants Foundation, the Advanced Machining Technology & Development Association, JST A-STEP Stage II (seed development type AS2915051S), and JSPS KAKENHI Grant Nos. JP19H02436 and 21K18830.

Data availability

Data will be made available on request.

References

[1] M.R. Derakhshandeh, M.J. Eshraghi, A. Jam, H. Rajaei, A. Fazili, Comparative studies on corrosion and tribological performance of multilayer hard coatings grown on WC-Co hardmetals, Int. J. Refract. Met. Hard Mater. 92 (2020) 105339, https://doi.org/10.1016/j.ijrmhm.2020.105339.
[2] A. Fazili, L. Nikzad, M.R. RahimiPour, M. Razavi, E. Salahi, Effect of Al2O3 ceramic binder on mechanical and microstructure properties of spark plasma sintered WC-Co cermets, Int. J. Refract. Met. Hard Mater. 69 (2017) 189–195, https://doi.org/10.1016/j.ijrmhm.2017.08.010.
[3] N. Geier, J.P. Davim, T. Szalay, Advanced cutting tools and technologies for drilling carbon fibre reinforced polymer (CFRP) composites: a review, Compos. A: Appl. Sci. Manuf. 125 (2019) 105552, https://doi.org/10.1016/j.compositesa.2019.105552.
[4] M.R. Derakhshandeh, M.J. Eshraghi, M. Razavi, Recent developments in the new generation of hard coatings applied on cemented carbide cutting tools, Int. J. Refract. Met. Hard Mater. 111 (2023) 106077, https://doi.org/10.1016/j.ijrmhm.2022.106077.
[5] X. Yan, H. Wang, X. Liu, C. Hou, Q. Qiu, X. Song, High-temperature oxidation and wear resistance of WC-Co based coatings with WB addition, J. Eur. Ceram. Soc. 39 (2019) 3023–3034, https://doi.org/10.1016/j.jeurceramsoc.2019.04.002.
[6] X. Ren, Z. Peng, Y. Peng, Z. Fu, C. Wang, L. Qi, H. Miao, Effect of SiC nano-whisker addition on WC–Ni based cemented carbides fabricated by hot-press sintering, Int. J. Refract. Met. Hard Mater. 36 (2013) 294–299, https://doi.org/10.1016/j.ijrmhm.2012.10.009.
[7] A. Fazili, M.R. Derakhshandeh, S. Nejadshamsi, L. Nikzad, M. Razavi, E. Ghasali, Improved electrochemical and mechanical performance of WC-Co cemented carbide by replacing a part of Co with Al2O3, J. Alloys Compd. 823 (2020) 153857, https://doi.org/10.1016/j.jallcom.2020.153857.

[8] S. Jia, W. Chen, J. Zhang, C.Y. Lin, H. Guo, G. Lu, K. Li, T. Zhai, Q. Ai, J. Lou, CVD growth of high-quality and large-area continuous h-BN thin films directly on stainless-steel as protective coatings, Materials Today Nano 16 (2021) 100135, https://doi.org/10.1016/j.mtnano.2021.100135.
[9] S. Hochstrasser-Kurz, D. Reiss, T. Suter, C. Latkoczy, D. Günther, S. Virtanen, P. Uggowitzer, P. Schmutz, ICP-MS, SKPFM, XPS, and microcapillary investigation of the local corrosion mechanisms of WC–Co hardmetal, J. Electrochem. Soc. 155 (2008) C415, https://doi.org/10.1149/1.2929822.
[10] A. Jam, S.M.R. Derakhshandeh, H. Rajaei, A.H. Pakseresht, Evaluation of microstructure and electrochemical behavior of dual-layer NiCrAlY/mullite plasma sprayed coating on high silicon cast iron alloy, Ceram. Int. 43 (2017) 14146–14155, https://doi.org/10.1016/j.ceramint.2017.07.155.
[11] A. Olayinka, A. Esther, O. Philip, Examination of electrochemical corrosion properties of titanium carbide thin film grown by RF magnetron sputtering, Materials Today: Proceedings 44 (2021) 994–999, https://doi.org/10.1016/j.matpr.2020.11.170.
[12] K. Yamamoto, M. Abdoos, P. Stolf, B. Beake, S. Rawal, G. Fox-Rabinovich, S. Veldhuis, Cutting performance of low stress thick TiAlN PVD coatings during machining of compacted graphite cast iron (CGI), Coatings 8 (2018) 38, https://doi.org/10.3390/coatings8010038.
[13] N. Schalk, M. Tkadletz, C. Mitterer, Hard coatings for cutting applications: physical vs. chemical vapor deposition and future challenges for the coatings community, Surf. Coat. Technol. 429 (2022) 127949, https://doi.org/10.1016/j.surfcoat.2021.127949.
[14] T.D. Howes, H.K. Tönshoff, W. Heuer, T. Howes, Environmental aspects of grinding fluids, CIRP Ann. 40 (1991) 623–630, https://doi.org/10.1016/S0007-8506(07)61138-X.
[15] A.A. Matei, I. Pencea, M. Branzei, D.E. Trancă, G. Ţepeş, C.E. Sfăt, E. Ciovica, A. I. Gherghilescu, G.A. Stanciu, Corrosion resistance appraisal of TiN, TiCN and TiAlN coatings deposited by CAE-PVD method on WC–Co cutting tools exposed to artificial sea water, Appl. Surf. Sci. 358 (2015) 572–578, https://doi.org/10.1016/j.apsusc.2015.08.041.
[16] L. Zhang, L. Shang, C. Gou, G. Zhang, Tribological and corrosive behavior under HCl corrosive environment of diamond-like carbon films with doped H, Cr and WC, Surf. Coat. Technol. 482 (2024) 130685, https://doi.org/10.1016/j.surfcoat.2024.130685.
[17] Q.-p. Wei, Z.M. Yu, M.N.R. Ashfold, L. Ma, Z. Chen, Fretting wear and electrochemical corrosion of well-adhered CVD diamond films deposited on steel substrates with a WC–Co interlayer, Diam. Relat. Mater. 19 (2010) 1144–1152, https://doi.org/10.1016/j.diamond.2010.04.004.
[18] G. Skordaris, K.D. Bouzakis, P. Charalampous, T. Kotsanis, E. Bouzakis, O. Lemmer, Effect of structure and residual stresses of diamond coated cemented carbide tools on the film adhesion and developed wear mechanisms in milling, CIRP Ann. 65 (2016) 101–104, https://doi.org/10.1016/j.cirp.2016.04.007.
[19] S. Fan, T. Kuang, W. Xu, Y. Zhang, Y. Su, S. Lin, D. Wang, H. Yang, K. Zhou, M. Dai, L. Wang, International Journal of Refractory Metals and Hard Materials, Effect of pretreatment strategy on the microstructure, mechanical properties and cutting performance of diamond coated hardmetal tools using HFCVD method 101 (2021) 105687, https://doi.org/10.1016/j.ijrmhm.2021.105687.
[20] G. Yan, Y. Wu, D. Cristea, F. Lu, Y. Wang, D. Zhao, M. Tierean, L. Liu, Results in Physics, Machining performance of hard-brittle materials by multi-layer micro-nano crystalline diamond coated tools 13 (2019) 102303, https://doi.org/10.1016/j.rinp.2019.102303.
[21] X.J. Li, L.L. He, Y.S. Li, Q. Yang, Surface and Coatings Technology, Catalytic graphite mechanism during CVD diamond film on iron and cobalt alloys in CH4-H2 atmospheres 360 (2019) 20–28, https://doi.org/10.1016/j.surfcoat.2018.12.120.
[22] X. Li, G. Liu, H. Gu, J. Orton, Cancer Genetics, Next-generation sequencing as a tool for precision medicine in clinical oncology 244 (2020) 11, https://doi.org/10.1016/j.cancergen.2020.04.032.
[23] J. Gao, H. Hei, K. Zheng, R. Wang, Y. Shen, X. Liu, B. Tang, Z. He, S. Yu, Journal of Alloys and Compounds, Design and synthesis of diffusion-modified HfC/HfCSiC bilayer system onto WC-Co substrate for adherent diamond deposition 705 (2017) 376–383, https://doi.org/10.1016/j.jallcom.2016.10.316.
[24] K. Ramasubramanian, N. Arunachalam, M.S. Ramachandra Rao, Surface and Coatings Technology, Investigation on tribological behaviour of boron doped diamond coated cemented tungsten carbide for cutting tool applications 332 (2017) 332–340, https://doi.org/10.1016/j.surfcoat.2017.06.090.
[25] Q. An, C. Wang, J. Xu, P. Liu, M. Chen, International Journal of Refractory Metals and Hard Materials, Experimental investigation on hard milling of high strength steel using PVD-AlTiN coated cemented carbide tool 43 (2014) 94–101, https://doi.org/10.1016/j.ijrmhm.2013.11.007.
[26] N. Khanna, J. Wadhwa, A. Pitroda, P. Shah, J. Schoop, M. Sarıkaya, Sustainable Materials and Technologies, Life cycle assessment of environmentally friendly initiatives for sustainable machining: a short review of current knowledge and a case study 32 (2022) e00413, https://doi.org/10.1016/j.susmat.2022.e00413.
[27] D. Griggs, M. Stafford-Smith, O. Gaffney, J. Rockström, M.C. Öhman, P. Shyamsundar, W. Steffen, G. Glaser, N. Kanie, I. Noble, Nature, Sustainable development goals for people and planet 495 (2013) 305–307, https://doi.org/10.1038/495305a.
[28] M.R. Diab, M. Egiza, K. Murasawa, H. Naragino, A. El-Shaer, T. Yoshitake, Eco-friendly thick and wear-resistant nanodiamond composite hard coatings deposited on WC–Co substrates, Surf. Coat. Technol. 479 (2024), https://doi.org/10.1016/j.surfcoat.2024.130517.
[29] A.M. Ali, T. Deckert-Gaudig, M. Egiza, V. Deckert, T. Yoshitake, Applied Physics Letters, Near- and far-field Raman spectroscopic studies of nanodiamond composite films deposited by coaxial arc plasma 116 (2020) 5, https://doi.org/10.1063/1.5142198.
[30] K. Hanada, T. Yoshida, Y. Nakagawa, T. Yoshitake, Japanese Journal of Applied Physics, Formation of ultrananocrystalline diamond/amorphous carbon composite films in vacuum using coaxial arc plasma gun 49 (2010), https://doi.org/10.1143/jjap.49.125503.
[31] K. Murasawa, M.R. Diab, H. Atta, H. Naragino, A. El-Shaer, T. Yoshitake, M. Egiza, Materials Today Communications, Disclosing mechanical and specific structural characteristics of thick and adherent nanodiamond composite hard coating deposited on WC−Co substrates 40 (2024), https://doi.org/10.1016/j.mtcomm.2024.109839.
[32] M. Egiza, M. Ragab Diab, A.M. Ali, K. Murasawa, T. Yoshitake, Materials Letters, Sustainable super-hard and thick nanodiamond composite film deposited on cemented carbide substrates with an interfacial Al-interlayer 364 (2024), https://doi.org/10.1016/j.matlet.2024.136369.
[33] M.A. Caro, V.L. Deringer, J. Koskinen, T. Laurila, G. Csányi, Growth mechanism and origin of High sp3 content in tetrahedral amorphous carbon, Phys. Rev. Lett. 120 (2018) 166101, https://doi.org/10.1103/PhysRevLett.120.166101.
[34] M. Egiza, A.M. Ali, M.R. Diab, N. Hemaya, K. Murasawa, T. Yoshitake, Surface and Coatings Technology, Synthesis and comprehensive synchrotron-based structural analysis of Si-doped nanodiamond composite films deposited on cemented carbide 471 (2023), https://doi.org/10.1016/j.surfcoat.2023.129867.
[35] M. Egiza, K. Murasawa, A.M. Ali, Y. Fukui, H. Gonda, M. Sakurai, T. Yoshitake, Japanese Journal of Applied Physics, Enhanced hardness of nanocarbon films deposited on cemented tungsten carbide substrates by coaxial arc plasma deposition owing to employing silicon-doped graphite targets 58 (2019), https://doi.org/10.7567/1347-4065/ab289f.
[36] M.R. Diab, M. Egiza, K. Murasawa, S. Ohmagari, H. Naragino, T. Yoshitake, Revealing mechanical and structural properties of Si-doped nanodiamond composite films through applied biasing voltages on WC−Co substrates, Int. J. Refract. Met. Hard Mater. (2024) 119, https://doi.org/10.1016/j.ijrmhm.2023.106518.
[37] M. Egiza, M.R. Diab, A.M. Ali, K. Murasawa, T. Yoshitake, Clean and durable thick nanodiamond composite hard coating deposited on cemented carbide towards sustainable machining: eco-friendly fabrication, characterization, and 3-E analysis, Cleaner Engineering and Technology 22 (2024), https://doi.org/10.1016/j.clet.2024.100804.
[38] H. Naragino, A. Tominaga, K. Hanada, T. Yoshitake, Applied Physics Express, Synthesis method for ultrananocrystalline diamond in powder employing a coaxial arc plasma gun 8 (2015), https://doi.org/10.7567/apex.8.075101.
[39] M. Egiza, M. Ragab Diab, H. Atta, M.M. Abdelfatah, A. El-Shaer, T. Yoshitake, Unveiling a 72.5 GPa peak hardness in sustainable nanodiamond composite hard coatings via discharge energy control: a nanoindentation-Raman approach, Mater. Lett. 369 (2024), https://doi.org/10.1016/j.matlet.2024.136684.
[40] W. Dai, Y. Shi, Q. Wang, J. Wang, Smooth diamond-like carbon films prepared by cathodic vacuum arc deposition with large glancing angles, Diam. Relat. Mater. 141 (2024) 110672, https://doi.org/10.1016/j.diamond.2023.110672.
[41] X. Li, L. He, Y. Li, Q. Yang, Catalytic graphite mechanism during CVD diamond film on iron and cobalt alloys in CH4-H2 atmospheres, Surf. Coat. Technol. 360 (2019) 20–28, https://doi.org/10.1016/j.surfcoat.2018.12.120.
[42] H. Naragino, M. Egiza, A. Tominaga, K. Murasawa, H. Gonda, M. Sakurai, T. Yoshitake, Japanese Journal of Applied Physics, Room-temperature hard coating of ultrananocrystalline diamond/nonhydrogenated amorphous carbon composite films on tungsten carbide by coaxial arc plasma deposition 55 (2016), https://doi.org/10.7567/jjap.55.030302.
[43] H. Naragino, M. Egiza, A. Tominaga, K. Murasawa, H. Gonda, M. Sakurai, T. Yoshitake, Applied Physics A, Hard coating of ultrananocrystalline diamond/nonhydrogenated amorphous carbon composite films on cemented tungsten carbide by coaxial arc plasma deposition 122 (2016), https://doi.org/10.1007/s00339-016-0284-4.
[44] J.T. Gudmundsson, A. Anders, A. von Keudell, Plasma Sources Science and Technology, Foundations of physical vapor deposition with plasma assistance 31 (2022), https://doi.org/10.1088/1361-6595/ac7f53.
[45] A.C. Ferrari, J. Robertson, Raman spectroscopy of amorphous, nanostructured, diamond–like carbon, and nanodiamond, Philos. Trans. R. Soc. London, Ser. A 362 (2004) 2477–2512, https://doi.org/10.1098/rsta.2004.1452.
[46] K. Hanada, T. Nishiyama, T. Yoshitake, K. Nagayama, Optical emission spectroscopy of deposition process of ultrananocrystalline diamond/hydrogenated amorphous carbon composite films by using a coaxial arc plasma gun, Diam. Relat. Mater. 19 (2010) 899–903, https://doi.org/10.1016/j.diamond.2010.02.019.
[47] J. Musil, Hard and superhard nanocomposite coatings, Surf. Coat. Technol. 125 (2000) 322–330, https://doi.org/10.1016/S0257-8972(99)00586-1.
[48] A.C. Ferrari, J. Robertson, Raman spectroscopy of amorphous, nanostructured, diamond-like carbon, and nanodiamond, Philos Trans A Math Phys Eng Sci 362 (2004) 2477–2512, https://doi.org/10.1098/rsta.2004.1452.
[49] A.C. Ferrari, J. Robertson, Origin of the 1150−cm−1 Raman mode in nanocrystalline diamond, Phys. Rev. B 63 (2001), https://doi.org/10.1103/PhysRevB.63.121405 (121405(R)).
[50] X. Song, M. Lu, H. Wang, X.C. Wang, F.H. Sun, Fracture mechanics of microcrystalline/nanocrystalline composited multilayer chemical vapor deposition self-standing diamond films, Ceram. Int. 48 (2022) 21868–21878, https://doi.org/10.1016/j.ceramint.2022.04.173.
[51] J. Peng, J. Zeng, Y. Xiao, W. Li, Novel conversion annealing pretreatment for improved deposition of diamond coatings onto WC-Co cemented carbide, J. Alloys Compd. 893 (2022) 162325, https://doi.org/10.1016/j.jallcom.2021.162325.

[52] B. Paramanik, D. Das, Synthesis of nanocrystalline diamond embedded diamond-like carbon films on untreated glass substrates at low temperature using (C2H2 + H2) gas composition in microwave plasma CVD, Appl. Surf. Sci. 579 (2022) 152132, https://doi.org/10.1016/j.apsusc.2021.152132.
[53] Q. Lin, S. Chen, Z. Ji, Z. Huang, Z. Zhang, B. Shen, Deposition of mirror-like surface finish ultrananocrystalline diamond films on tungsten carbide by optimizing the substrate pretreatment, Surf. Coat. Technol. 394 (2020) 125885, https://doi.org/10.1016/j.surfcoat.2020.125885.
[54] A. Dychalska, P. Popielarski, W. Franków, K. Fabisiak, K. Paprocki, M.J.M.S.-P. Szybowicz, Study of CVD diamond layers with amorphous carbon admixture by Raman scattering spectroscopy 33 (2015) 799–805, https://doi.org/10.1515/MSP-2015-0067.
[55] K. Aoki, K. Suzuki, K. Ishii, K. Takanashi, T. Komukai, K. Oura, T. Hirao, Formation of nanoscale diamond particles without substrate heating by cathodic arc deposition, Jpn. J. Appl. Phys. 44 (2005), https://doi.org/10.1143/jjap.44.L746.
[56] I.I. Vlasov, V.G. Ralchenko, E. Goovaerts, A.V. Saveliev, M.V. Kanzyuba, Bulk and surface-enhanced Raman spectroscopy of nitrogen-doped ultrananocrystalline diamond films, Phys. Stat. Sol. (A) 203 (2006) 3028–3035, https://doi.org/10.1002/pssa.200671119.
[57] I. Harada, Y. Furukawa, M. Tasumi, H. Shirakawa, S. Ikeda, Spectroscopic studies on doped polyacetylene and β-carotene, J. Chem. Phys. 73 (2008) 4746–4757, https://doi.org/10.1063/1.440007.
[58] P.S. Martins, P.A. Almeida Magalhães Júnior, J.R. Gonçalves Carneiro, E.C. Talibouya Ba, V.F. Vieira, Study of diamond-like carbon coating application on carbide substrate for cutting tools used in the drilling process of an Al–Si alloy at high cutting speeds, Wear 498–499 (2022) 204326, https://doi.org/10.1016/j.wear.2022.204326.
[59] A. Rosenkranz, L. Freeman, S. Fleischmann, F. Lasserre, Y. Fainman, F.E. Talke, Tip-enhanced Raman spectroscopy studies of nanodiamonds and carbon onions, Carbon 132 (2018) 495–502, https://doi.org/10.1016/j.carbon.2018.02.088.
[60] R. Dumpala, N. Kumar, C.R. Kumaran, S. Dash, B. Ramamoorthy, M. S. Ramachandra Rao, Adhesion characteristics of nano- and micro-crystalline diamond coatings: Raman stress mapping of the scratch tracks, Diam. Relat. Mater. 44 (2014) 71–77, https://doi.org/10.1016/j.diamond.2014.02.007.
[61] H. Cicek, A. Keles, Y. Totik, I. Efeoglu, Adhesion and multipass scratch characterization of Ti:Ta-DLC composite coatings, Diam. Relat. Mater. 83 (2018) 80–86, https://doi.org/10.1016/j.diamond.2018.02.002.
[62] A.M. Ali, M. Egiza, K. Murasawa, H. Sugita, T. Deckert-Gaudig, V. Deckert, T. Yoshitake, Effects of substrate temperature and intermediate layer on adhesion, structural and mechanical properties of coaxial arc plasma deposition grown nanodiamond composite films on Si substrates, Surf. Coat. Technol. 417 (2021) 11, https://doi.org/10.1016/j.surfcoat.2021.127185.
[63] N. Vidakis, A. Antoniadis, N. Bilalis, The VDI 3198 indentation test evaluation of a reliable qualitative control for layered compounds, J. Mater. Process. Technol. 143–144 (2003) 481–485, https://doi.org/10.1016/s0924-0136(03)00300-5.
[64] K. Wegener, F. Kuster, S. Weikert, L. Weiss, J. Stirnimann, Success story cutting, Procedia CIRP 46 (2016) 512–524, https://doi.org/10.1016/j.procir.2016.04.110.
[65] E. Westkämper, Alting, Arndt, CIRP Ann., Life cycle management and assessment: approaches and visions towards sustainable manufacturing (keynote paper), 49 (2000) 501–526. doi:https://doi.org/10.1016/S0007-8506(07)63453-2.
[66] M. Egiza, M.R. Diab, A.M. Ali, K. Murasawa, T. Yoshitake, Clean and durable thick nanodiamond composite hard coating deposited on cemented carbide towards sustainable machining: eco-friendly fabrication, characterization, and 3-E analysis, Cleaner Engineering and Technology 22 (2024) 100804, https://doi.org/10.1016/j.clet.2024.100804.
[67] H. Parangusan, J. Bhadra, N. Al-Thani, A review of passivity breakdown on metal surfaces: influence of chloride- and sulfide-ion concentrations, temperature, and pH, Emergent Materials 4 (2021) 1187–1203, https://doi.org/10.1007/s42247-021-00194-6.
[68] L. Liu, J. Xu, Z.-H. Xie, P. Munroe, The roles of passive layers in regulating the electrochemical behavior of Ti5Si3-based nanocomposite films, J. Mater. Chem. A 1 (2013) 2064–2078, https://doi.org/10.1039/C2TA00510G.
[69] R. Dumpala, M. Chandran, N. Kumar, S. Dash, B. Ramamoorthy, M.S.R. Rao, Growth and characterization of integrated nano- and microcrystalline dual layer composite diamond coatings on WC–Co substrates, Int. J. Refract. Met. Hard Mater. 37 (2013) 127–133, https://doi.org/10.1016/j.ijrmhm.2012.11.007.
[70] M.R. Diab, K. Murasawa, A.M.M. Ibrahim, H. Naragino, T. Yoshitake, M. Egiza, Wear-resistant and stable low-friction nanodiamond composite superhard coatings against Al2O3 counter-body in dry condition, Int. J. Refract. Met. Hard Mater. 126 (2025) 106955, https://doi.org/10.1016/j.ijrmhm.2024.106955.
[71] K.-J. Feng, C.-Q. Guo, S.-S. Lin, Z.-Q. Fu, Q. Shi, Y.-F. Su, W. Wang, M.-J. Dai, Structure and properties of ta-C films prepared by vacuum cathodic arc with an unbalanced external electromagnetic field, Ceram. Int. 48 (2022) 111–119, https://doi.org/10.1016/j.ceramint.2021.09.086.
[72] L. Aihua, D. Jianxin, C. Haibing, C. Yangyang, Z. Jun, Friction and wear properties of TiN, TiAlN, AlTiN and CrAlN PVD nitride coatings, Int. J. Refract. Met. Hard Mater. 31 (2012) 82–88, https://doi.org/10.1016/j.ijrmhm.2011.09.010.
[73] X. Liu, H. Zhang, T. Zhu, G. Lin, H. Shi, D. Diao, Effect of substrate bias on microstructure, mechanical and tribological properties of amorphous carbon films fabricated by electron cyclotron resonance ion irradiation, Ceram. Int. 50 (2024) 31088–31096, https://doi.org/10.1016/j.ceramint.2024.05.414.
[74] G.M. Krolczyk, R.W. Maruda, J.B. Krolczyk, S. Wojciechowski, M. Mia, P. Nieslony, G. Budzik, Ecological trends in machining as a key factor in sustainable production – a review, J. Clean. Prod. 218 (2019) 601–615, https://doi.org/10.1016/j.jclepro.2019.02.017.
[75] F. Koné, C. Czarnota, B. Haddag, M. Nouari, Modeling of velocity-dependent chip flow angle and experimental analysis when machining 304L austenitic stainless steel with groove coated-carbide tools, J. Mater. Process. Technol. 213 (2013) 1166–1178, https://doi.org/10.1016/j.jmatprotec.2013.01.015.
[76] K.-L. Choy, Chemical Vapour Deposition (CVD): Advances, Technology and Applications, CRC Press, 2019, https://doi.org/10.1201/9780429342363 (1000690733).
[77] M. Barletta, G. Rubino, A. Gisario, Adhesion and wear resistance of CVD diamond coatings on laser treated WC–Co substrates, Wear 271 (2011) 2016–2024, https://doi.org/10.1016/j.wear.2011.01.042.
[78] A. Merlo, G. Leonard, Magnetron sputtering vs. electrodeposition for hard chrome coatings: a comparison of environmental and economic performances, Materials (Basel) 14 (2021), https://doi.org/10.3390/ma14143823.
[79] Z. Yuan, Y. Guo, C. Li, L. Liu, B. Yang, H. Song, Z. Zhai, Z. Lu, H. Li, T. Staedler, N. Huang, X. Jiang, New multilayered diamond/β-SiC composite architectures for high-performance hard coating, Mater. Des. 186 (2020) 108207, https://doi.org/10.1016/j.matdes.2019.108207.
[80] K. Murasawa, M.R. Diab, M. Wang, H. Naragino, T. Yoshitake, M. Egiza, Influence of droplet-free ta-C coatings and lubrication conditions on tribological performance and mechanical characteristics of WC−Co, Mater. Lett. 372 (2024) 137058, https://doi.org/10.1016/j.matlet.2024.137058.
[81] M. Gassner, M. Rebelo de Figueiredo, N. Schalk, R. Franz, C. Weiß, H. Rudigier, H. Holzschuh, W. Bürgin, M. Pohler, C. Czettl, C. Mitterer, Energy consumption and material fluxes in hard coating deposition processes, Surf. Coat. Technol. 299 (2016) 49–55, https://doi.org/10.1016/j.surfcoat.2016.04.062.